Water Maser Survey on AKARI and IRAS Sources: A Search for "Low-velocity" Water Fountains

The Astrophysical Journal, 769:20 (18pp), 2013 May 20 doi:10.1088/0004-637X/769/1/20

WATER MASER SURVEY ON *AKARI* AND *IRAS* SOURCES: A SEARCH FOR "LOW-VELOCITY" WATER FOUNTAINS

Bosco H. K. Yung[1], Jun-ichi Nakashima[1], Hiroshi Imai[2], Shuji Deguchi[3], Christian Henkel[4,5], and Sun Kwok[1]
[1] Department of Physics, The University of Hong Kong, Pokfulam Road, Hong Kong, China
[2] Graduate School of Science and Engineering, Kagoshima University, 1-21-35 Korimoto, Kagoshima 890-0065, Japan
[3] Nobeyama Radio Observatory, National Astronomical Observatory of Japan, Minamimaki, Minamisaku, Nagano 384-1305, Japan
[4] Max-Planck-Institut für Radioastronomie, Auf dem Hügel 69, D-53121 Bonn, Germany
[5] Astron. Dept., King Abdulaziz University, P.O. Box 80203, Jeddah, Saudi Arabia
Received 2012 November 1; accepted 2013 March 6; published 2013 May 1

ABSTRACT

We present the results of a 22 GHz H_2O maser survey toward a new sample of asymptotic giant branch (AGB) and post-AGB star candidates. Most of the objects are selected for the first time based on the *AKARI* data, which have high flux sensitivity in the mid-infrared ranges. We aim at finding H_2O maser sources in the transient phase between the AGB and post-AGB stages of evolution, where the envelopes start to develop large deviations from spherical symmetry. The observations were carried out with the Effelsberg 100 m radio telescope. Among 204 observed objects, 63 detections (36 new) were obtained. We found four objects that may be "water fountain" sources (IRAS 15193+3132, IRAS 18056−1514, OH 16.3−3.0, and IRAS 18455+0448). They possess an H_2O maser velocity coverage much smaller than those in other known water fountains. However, the coverage is still larger than that of the 1612 MHz OH maser. It implies that there is an outflow with a higher velocity than the envelope expansion velocity (typically $\leqslant$25 km s^{-1}), meeting the criterion of the water fountain class. We suggest that these candidates are possibly oxygen-rich late AGB or early post-AGB stars in a stage of evolution immediately after the spherically symmetric AGB mass loss has ceased.

Key words: infrared: stars – masers – stars: AGB and post-AGB – stars: evolution – stars: winds, outflows

Online-only material: color figures, machine-readable table

1. INTRODUCTION

The circumstellar envelopes of oxygen-rich asymptotic giant branch (AGB) stars are well-known emitters of OH, H_2O, and SiO masers. In particular, 22 GHz H_2O masers mainly occur in the region beyond the dust formation zone. Their spectral profiles are sensitive to the mass-loss rate as well as to the geometry of the envelopes (e.g., Engels et al. 1986; Likkel et al. 1992). Thus, by observing H_2O masers we are able to study in detail the kinematics of the envelopes of evolved stars, which are usually optically opaque in short wavelengths.

Maser surveys are commonly performed by single-dish radio telescopes. However, prior to the launching of the *Infrared Astronomical Satellite* (*IRAS*), selecting suitable observing targets was not easy due to limited methods for identifying evolutionary status. The efficiency has been improved after van der Veen & Habing (1988) suggested the stellar classification method using the *IRAS* two-color diagram, and since then *IRAS* colors have become a main criterion used in source selection for many maser surveys. The color used is defined as $[m]-[n] = 2.5\log(F_n/F_m)$, where F_m and F_n represent the fluxes at the m and n μm bands, respectively. The H_2O maser survey reported by Engels & Lewis (1996) was a notable early example using the *IRAS* Point Source Catalog. The authors selected over 300 OH/IR stars, which are oxygen-rich late AGB stars with very thick envelopes, based on their *IRAS* [12]−[25] and [25]−[60] colors. They achieved a detection rate of up to ∼50% using the Effelsberg 100 m radio telescope, and the results demonstrated the effectiveness of the color selection method. Another large-scale H_2O maser survey was reported by Lewis (1997), but here the author focused on color-selected Mira variables instead of OH/IR stars. Eighteen new detections were found from ∼200 objects. The Haystack 37 m radio telescope was used for this observation. A few more H_2O maser surveys carried out before the year 2000 are summarized in the Arcetri Catalog (Valdettaro et al. 2001 and references therein); all of the sources in the catalog were observed with the Medicina 32 m radio telescope. A recent notable survey of similar nature was conducted by Deacon et al. (2007). This time the target of interest shifted to post-AGB stars. Their searched objects included 85 post-AGB stars selected by 1612 MHz OH maser properties and *IRAS* colors. The Tidbinbilla 70 m radio telescope was used for maser observation, and 21 detections were obtained. The most important result from Deacon et al. (2007) was the discovery of three new "water fountain" (WF) sources. There were nine more post-AGB H_2O maser sources reported by Suárez et al. (2007, 2009), which also included two new WFs.

WFs are mainly oxygen-rich late AGB or post-AGB stars exhibiting high-velocity collimated bipolar outflows (or jets) traced by H_2O maser emission (e.g., Imai et al. 2012). They are suggested to be transitional objects and their jets contribute to the shaping of planetary nebulae (PNe; see Imai 2007; Desmurs 2012 for a review). The velocities of their bipolar outflows are larger than those of the slowly expanding envelopes, which are the remains from the mass loss during the AGB phase. In a typical AGB star, the 1612 MHz OH masers show a double-peaked line shape. Each peak reveals the velocity of the approaching blueshifted or the receding redshifted side of the expanding envelope. OH masers are found beyond the accelerating region, in an environment where the expansion motion reaches terminal velocity (typically 5–25 km s^{-1}; te Lintel Hekkert et al. 1989). H_2O masers, on the other hand, mainly show two types of line profiles. In AGB stars with lower mass loss (e.g., Mira variables), the masers show a single emission peak close to the systemic velocity, but in the high

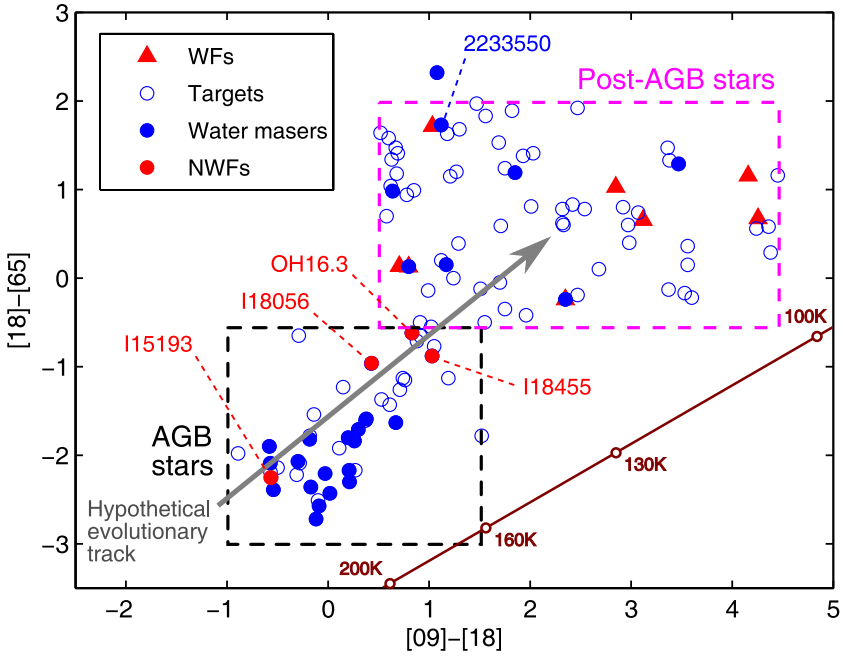

Figure 1. *AKARI* two-color diagram showing the objects observed in the present survey (open blue circles), the H_2O maser detections (filled blue circles), the water fountains known to date (WFs; red triangles), and the newly identified WF candidates (NWFs; filled red circles). The blackbody curve is indicated by the brown solid line. The estimated boundaries for AGB and post-AGB stars are shown in broken-line boxes. A hypothetical evolutionary track is shown by the gray arrow.

(A color version of this figure is available in the online journal.)

mass-loss cases (e.g., OH/IR stars), a double-peaked profile is observed, similar to that of the OH masers (Takaba et al. 1994). In both cases, an H_2O maser spectral profile would have a smaller velocity coverage than that of OH. For WFs, on the contrary, due to the high-velocity (bipolar) outflows, the spectral velocity coverage of H_2O is larger than that of OH. WFs are rare objects; to date there are only 15 confirmed members (Desmurs 2012). Notable examples include IRAS 16342−3814 (Sahai et al. 1999; Claussen et al. 2009), W43A (Imai et al. 2002) and IRAS 18286−0959 (Yung et al. 2011). Most of the WFs are found to be post-AGB stars, with the only possible exceptions of W43A and OH 12.8−0.9 (Boboltz & Marvel 2005, 2007), which may be late AGB stars.

The H_2O maser spectral velocity coverage of WFs are often very large (even $\geqslant$100 km s^{-1}). However, a spectrum can only reveal the line-of-sight velocity of the jet. The velocity coverage is affected by the inclination angle between the jet axis and the line of sight. If the outflow direction is nearly perpendicular to it, the maser emission peaks will show only a small velocity separation in a spectrum, even if the jet has a high three-dimensional velocity. In fact, OH 12.8−0.9 is the WF with the smallest H_2O velocity coverage ($\sim$50 km s^{-1}), but upon interferometric observations, bipolar outflow is revealed (Boboltz & Marvel 2005, 2007). Therefore, some of those "low-velocity" sources that have been misidentified as typical AGB stars are probably WFs as well. The smaller velocity coverage can be explained by either a high-velocity jet close to the plane of the sky, or the objects really possessing a slow jet. There have been no studies really focusing on these possibilities.

In this paper, we present the results of a new H_2O maser survey on objects selected not only from *IRAS*, but also from the relatively new *AKARI* database which is characterized by a much higher sensitivity (see Section 2.1). We aim at finding H_2O masers associated with the aforementioned transitional objects and found four WF candidates that possess even smaller velocity coverage (30–40 km s^{-1}) than OH 12.8−0.9. Their expansion velocities are just slightly larger than those for normal AGB stars ($<$30 km s^{-1}). Thus, without a comparison with OH (i.e., the H_2O velocity coverage should be larger than that for OH), it is difficult to claim they could be WFs. We suggest that the above "low-velocity" WF candidates have probably reached the late AGB or very early post-AGB phase, which is supported by their location in the *AKARI* two-color diagram (Section 5.2).

The details of the *AKARI* two-color diagram, sample selection, and the observation in this work are given in Sections 2 and 3. The results are reported in Section 4, followed by the discussion in Section 5.

2. SAMPLE SELECTION

2.1. AKARI Two-color Diagram

Most of the observed objects were selected from the *AKARI* and *IRAS* databases. The *AKARI* data were released in two catalogs.[6] The 9 and 18 μm band fluxes are given in the Infrared Camera (IRC) Point Source Catalog, which contains 427,071 objects (Kataza et al. 2010); the 65, 90, 140, and 160 μm band fluxes are given in the Far-Infrared Surveyor (FIS) Bright Source Catalog, which contains 870,973 objects (Yamamura et al. 2010). We have used the 9, 18 and 65 μm band fluxes for object selection because these bands have better sensitivity—down to 0.045 and 0.06 Jy at 9 and 18 μm, respectively (Kataza et al. 2010). The band sensitivity at 65 μm is not given in the catalog release note, but that at 90 μm is given as 0.55 Jy. For a comparison, the *IRAS* sensitivities are about 0.5 Jy at 12, 25, and 60 μm, and 1 Jy at 100 μm.

Using known sources, we define the empirical regions of AGB and post-AGB stars on a two-color diagram with *AKARI* [09]−[18] and [18]−[65] colors (Figure 1). The known AGB stars (including Mira variables and OH/IR stars) with H_2O maser detections are selected from Engels et al. (1986), Engels

[6] http://www.ir.isas.jaxa.jp/AKARI/Observation/PSC/Public/

Table 1
Parameters of the Observing Targets

Object	R.A.[a]	Decl.[a]	IC_{12}[b]	IC_{23}[b]	AC_{12}[c]	AC_{23}[c]	OH $V_{b,p}$[d] (km s^{-1})	OH $V_{r,p}$[d] (km s^{-1})	Ref. 1[e]	SiO V_{LSR} 1[f] (km s^{-1})	SiO V_{LSR} 2[f] (km s^{-1})	Ref. 2[g]	Cat.[h]
IRAS 23575+2536	00 00 06.56	+25 53 11.2	−0.94	−2.08	−0.83	...	N	N	1	−29.2	−29.1	2	e
IRAS 00170+6542	00 19 51.28	+65 59 30.4	0.19	−1.68	0.26	−1.84	−65.0	−37.6	3	−48.9	−51.0	4	d,e
V 524CAS	00 46 00.12	+69 10 53.4	−0.36	−1.78	−0.09	−2.57	−34.8	−16.5	5	−27.0	...	6	c,e
IRAS 01572+5844	02 00 44.10	+58 59 03.0	−0.50	−1.86	...	...	−19.8	−2.9	7	...	...	...	d
IRAS 02547+1106	02 57 27.48	+11 18 05.7	−0.09	−1.71	−0.31	−2.22	6.4	25.4	1	...	...	...	c,d
IRAS 03022+5409	03 05 52.91	+54 20 53.9	−0.43	−2.18	−0.30	...	...	...	...	N	N	8	d,e
IRAS 03206+6521	03 25 08.80	+65 32 07.0	0.36	−1.38	0.71	−1.26	−47.0	−28.0	3	−40	−37.8	6, 9	b,d,e
IRAS 03461+6727	03 50 57.00	+67 36 50.0	−0.74	−1.60	−0.64	...	...	...	...	...	...	...	f
IRAS 04209+4800	04 24 40.40	+48 07 24.2	−0.28	−1.91	−0.57	−2.09	−26.4	...	7	−16.8	−16.7	9	c,d,e
IRAS 05131+4530	05 16 47.10	+45 34 04.0	0.61	−1.29	0.61	−1.43	−42.8	−22.9	3	N	−30.5	8	c,d,e

Notes.
[a] J2000.0.
[b] IC_{12} and IC_{23} represent the *IRAS* [12]−[25] and [25]−[60] colors, respectively.
[c] AC_{12} and AC_{23} represent the *AKARI* [09]−[18] and [18]−[65] colors, respectively.
[d] $V_{b,p}$ and $V_{r,p}$ represent the V_{LSR} of the blueshifted and redshifted peak of a double-peaked 1612 MHz OH maser profile, respectively. For a single-peaked profile, the V_{LSR} is recorded as $V_{b,p}$, whether or not it is really "blueshifted." Non-detection is denoted by "N."
[e] References for 1612 MHz OH maser velocities.
[f] "SiO V_{LSR} 1" and "SiO V_{LSR} 2" represent the V_{LSR} of the SiO maser peak in the ($v = 1$, $J = 1$–0) and ($v = 2$, $J = 1$–0) transitions, respectively. Non-detection is denoted by "N."
[g] References for SiO maser velocities.
[h] Category, from (a) to (g), in which the object belongs to.
[i] From our unpublished data of an OH maser observation conducted in year 2012, using the Effelsberg 100 m radio telescope.
[j] Imai et al. (2005) found that W43A actually has a biconical flow traced by SiO emission. The spectral velocity range is from about 15–50 km s^{-1}.
References. (1) Lewis 1994; (2) Cho & Ukita 1996; (3) Le Squeren et al. 1992; (4) Fujii 2001; (5) Szymczak & Le Squeren 1995; (6) Pointing list of the NRO 45 m telescope; (7) Sivagnanam et al. 1990; (8) Jiang et al. 1999; (9) Jiang et al. 1996; (10) David et al. 1993; (11) Zapata et al. 2009; (12) Lewis et al. 1995; (13) Jewell et al. 1991; (14) Deguchi et al. 2004; (15) Kim et al. 2010; (16) Ita et al. 2001; (17) te Lintel Hekkert 1991b; (18) te Lintel Hekkert 1991a; (19) Deguchi et al. 2010; (20) Szymczak & Gerard 2004; (21) Nyman et al. 1998; (22) Payne et al. 1998; (23) Deguchi et al. 2000; (24) Izumiura et al. 1999; (25) Engels & Jimenez-Esteban 2007; (26) Nakashima & Deguchi 2003a; (27) Sivagnanam & Le Squeren 1988; (28) Matsuura et al. 2000; (29) Imai et al. 2008; (30) Deguchi et al. 2007; (31) Sevenster et al. 2001; (32) te Lintel Hekkert et al. 1989; (33) Lewis et al. 2001; (34) Nakashima & Deguchi 2003b; (35) Eder et al. 1988; (36) Chengalur et al. 1993; (37) Hu et al. 1994; (38) Lewis et al. 1987; (39) Gledhill et al. 2001; (40) Josselin et al. 1998; (41) Lewis et al. 1990; (42) Engels 1996; (43) Likkel 1989; (44) Nakashima et al. 2011; (45) Nakashima & Deguchi 2007; (46) te Lintel Hekkert & Chapman 1996; (47) Lepine et al. 1978; (48) Deguchi et al. 2005; (49) Galt et al. 1989.

(This table is available in its entirety in a machine-readable form in the online journal. A portion is shown here for guidance regarding its form and content.)

& Lewis (1996), Lewis (1997), and Valdettaro et al. (2001). A total of 265 sources are selected. The boundaries are set by the outermost AGB stars distributed on the diagram. For simplicity, a rectangular region is assumed. The same process is used to find out the color region of post-AGB stars. We use 38 post-AGB stars with H_2O maser detections to define the color region. In this sample, 30 of them are selected from Deacon et al. (2007) and Suárez et al. (2007, 2009). The remaining eight are the WFs. They are selected because most WFs appear to be post-AGB stars (see Section 1). Note that only eight WFs have known *AKARI* fluxes. Therefore, we cannot include all 15 in the *AKARI* color–color diagram. Post-AGB stars have a much lower H_2O maser detection rate (see Section 4.1), and there were also not that many corresponding observations, and hence we could only obtain the smaller sample.

2.2. Categories of Observed Objects

A total of 204 observed objects were selected using different criteria in addition to the empirical regions of the *AKARI* two-color diagram introduced in Section 2.1. In Table 1, the objects are put into categories (a)–(h), according to their nature. Note that some objects can fall into more than one category.

Category (a). Contains potential WFs and known WFs. As mentioned in Section 1, the difference between H_2O and OH velocity coverages is a key point to distinguish WFs from other AGB/post-AGB stars. Potential WFs are objects for which previous observations show almost equal velocity coverage of H_2O and OH masers (see the references in Table 1). These marginal cases might turn out to be WFs once extra H_2O maser components are observed at higher velocities. There are 15 objects included.

Categories (b) and (c). The former category contains *AKARI* objects (Decl. $\geqslant -20^\circ$) lying inside the post-AGB region in the *AKARI* two-color diagram (Figure 1), with $0.5 \leqslant [09]-[18] \leqslant 4.5$ and $-0.5 \leqslant [18]-[65] \leqslant 2$. The latter is similar but for the AGB region in the same diagram, with $-1 \leqslant [09]-[18] \leqslant 1.5$ and $-3 \leqslant [18]-[65] \leqslant -0.5$ (Figure 1). There are about 350 and 470 objects fulfilling the above criteria for (b) and (c), respectively. However, due to the limited observing time, we selected only those which are relatively bright in 9 μm (>3 Jy). There are finally 68 and 38 objects included.

Category (d). Contains *IRAS* objects (Decl. $\geqslant -20^\circ$) selected from the AGB, post-AGB, or redder regions (i.e., IIIa, IIIb, IV, V, and VIII) of the *IRAS* two-color diagram studied by van der Veen & Habing (1988), as shown in Figure 2. The selection method is similar to previous surveys like that of Engels & Lewis (1996), but new samples are added. There are about 360 objects fulfilling the above criteria. We selected only those which are relatively bright in 12 μm (>5 Jy). There are finally 106 objects included.

Category (e). Contains known SiO maser sources not observed at 22 GHz before. SiO masers are often detected in oxygen-rich envelopes. These objects are most likely AGB to very early post-AGB stars. There are 98 objects included.

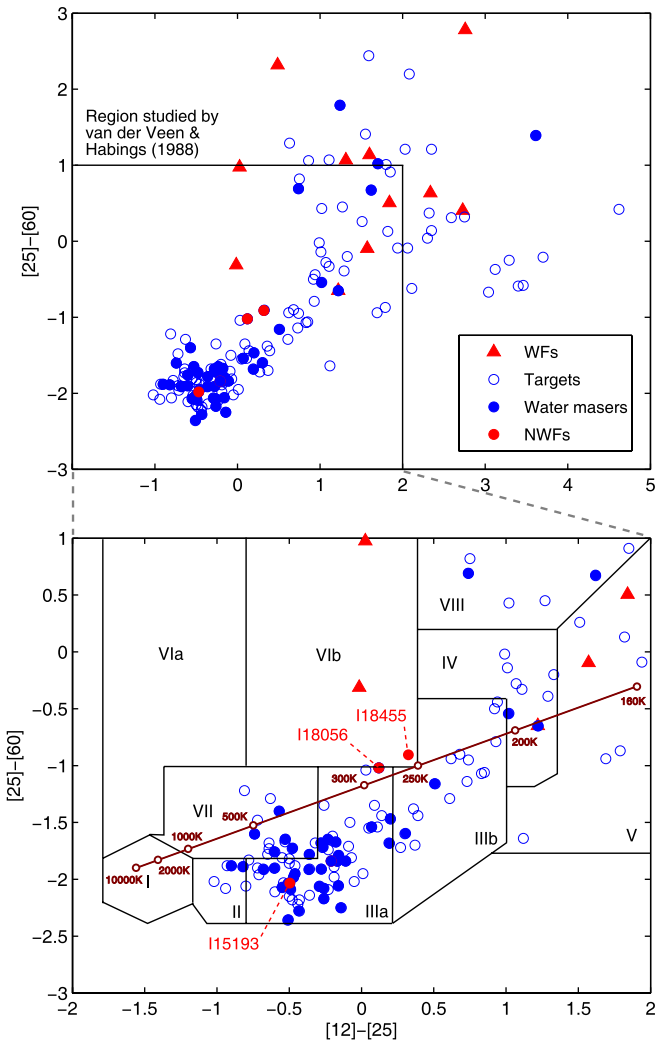

Figure 2. Upper panel: *IRAS* two-color diagram showing the objects observed in the present survey (open blue circles), the H_2O maser detections (filled blue circles), the water fountains known to date (WFs; red triangles), and three of the newly found WF candidates (NWFs; filled red circles). We do not have sufficient information on the *IRAS* flux of OH 16.3−3.0, the fourth candidate, thus its position on this diagram is not known. Lower panel: enlarged view of the region studied by van der Veen & Habing (1988). A blackbody curve is indicated by the brown solid line.

(A color version of this figure is available in the online journal.)

Categories (f) and (g). Contains H_2O non-detections in two previous major surveys. Category (f) refers to Lewis (1997), and category (g) to Johnston et al. (1973). As masers show variability, it often happens that previous non-detections become new detections upon re-observation some years later. Therefore it is worth revisiting some of these objects. It was due to limited observing time that only six objects were observed.

Categories (h). Contains other sources that do not belong to any of the above categories. These are mainly previously observed objects selected from one of the references for re-observation (see Table 1). There are five objects included.

The columns of Table 1 contain the following information:

Column 1. Object name.

Columns 2 and 3. R.A. and Decl. in J2000.0.

Columns 4 and 5. IRAS [12]−[25] and [25]−[60] colors, respectively.

Columns 6 and 7. AKARI [09]−[18] and [18]−[65] colors, respectively.

Column 8. The local standard-of-rest velocity (V_{LSR}) of the blueshifted peak of a double-peaked 1612 MHz OH maser profile. For a single-peaked profile, the V_{LSR} is recorded in this column as well, whether or not it is really "blueshifted".

Column 9. V_{LSR} of the redshifted peak of a double-peaked 1612 MHz OH maser profile.

Column 10. References for the OH maser information given in Columns 8 and 9.

Columns 11 and 12. V_{LSR} of the SiO maser peak in the ($v = 1$, $J = 1$–0) and ($v = 2$, $J = 1$–0) transitions, respectively.

Column 13. References for the SiO maser information given in Columns 11 and 12.

Column 14. Category, from (a) to (g), to which the object belongs.

3. OBSERVATION AND DATA REDUCTION

The observation was performed with the Effelsberg 100 m radio telescope from 2011 November 30 to December 6. An 18–26 GHz HEMT receiver and fast Fourier transform spectrometer were used in the front end and the back end, respectively. The rest frequency of the $6_{16} \rightarrow 5_{23}$ transition line of H_2O molecules was adopted as 22.235080 GHz (Lovas 2004). At this frequency, the FWHM of the beam was about 40″. A 500 MHz bandwidth was used to cover a frequency range from 21.985 to 22.485 GHz (~6700 km s^{-1} at 22.2 GHz). The number of spectral channels was 16,384, yielding a channel spacing of ~0.4 km s^{-1}. The velocity resolution corresponded to two channels, i.e., ~0.8 km s^{-1}, which was sufficient to spectroscopically resolve each water maser component (normally with a line width of ~1–2 km s^{-1}). By using the 500 MHz bandwidth, we were able to also detect the H66α (with rest frequency 22.364 GHz) and H83β (22.196 GHz) recombination lines for certain objects (see Section 4.2 and the Appendix). The velocity scale has been confirmed to be accurate by comparisons with previous H_2O maser spectra of some known sources.

An ON/OFF cycle of 2 minutes was used in position switching mode. The OFF position was 600″ west from the ON position in the azimuthal direction. The observing time for each source was about 6–20 minutes. The weather was fine during most of the observing sessions, and the rms noise level was of order 10^{-2} to 10^{-3} Jy. Pointing was obtained every 1–2 hr with a typical accuracy of about 5″. Calibration was obtained from continuum cross scans of sources with flux densities given by Ott et al. (1994).

The data reduction procedures were performed with the Continuum and Line Analysis Single-dish Software (CLASS) package.[7] Individual scans on each object were inspected and those with obvious artifacts were discarded. The remaining scans were then averaged. The baseline of each spectrum was fit by a one-degree polynomial and subtracted, using the channels without emission.

4. RESULTS

4.1. H_2O Maser Detections

In this observation, we obtained a total of 63 detections out of 204 objects, and 36 of them are new. Table 2 gives the number of detections in each selection category (see Section 2.2 and the last column of Table 1). Figure 3 shows the spectra for all new detections, and Figure 4 shows the spectra for revisited known

[7] http://www.iram.fr/IRAMFR/GILDAS

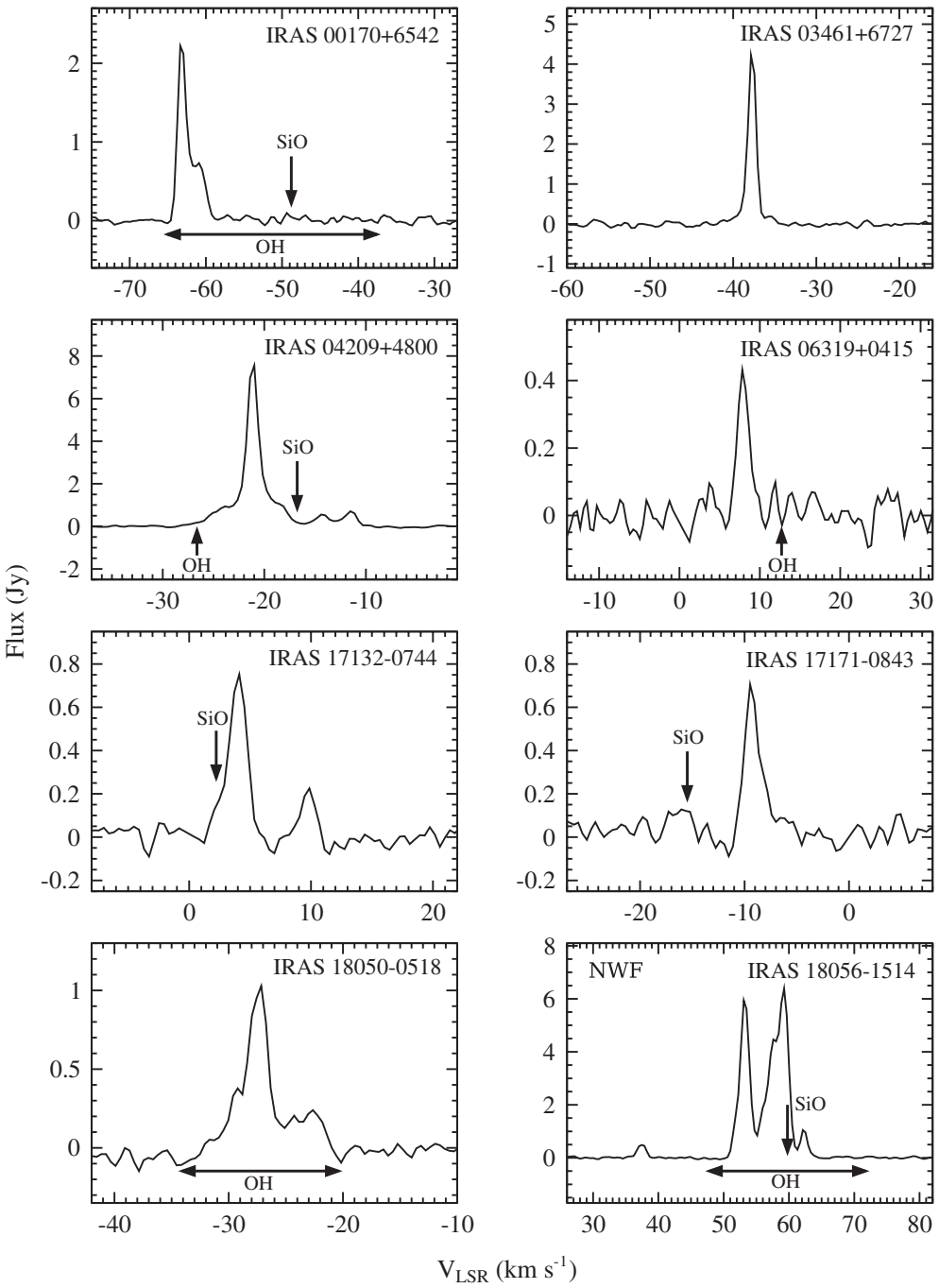

Figure 3. Spectra of new H_2O maser detections. The new "low-velocity" water fountain candidates (IRAS 18056−1514, OH 16.3−3.0 and IRAS 18455+0448) are labeled "NWF."

Table 2
Number of H_2O Maser Detections in Each Category Described in Section 2.2.

Category	Objects Observed	New Masers	Known Masers
a	15	0	15
b	68	6	3
c	38	11	5
d	106	21	16
e	98	22	14
f	1	1	0
g	5	3	0
h	5	0	1

maser sources. When possible, the velocity range between the two OH maser peaks and the V_{LSR} of the SiO maser feature (if present) are also shown. The parameters of all the H_2O maser detections are given in Table 3. The rms noise level of the non-detections are then given in Table 4.

The new attempt at sample selection using *AKARI* colors yields a detection rate of 42% for AGB stars (category (c)), but only about 13% for post-AGB stars (category (b)). This drastic drop of the detection rate toward redder post-AGB stars is expected, and the same tendency was observed in nearly all previous H_2O maser surveys on evolved stars (e.g., Engels & Lewis 1996; Valdettaro et al. 2001). It is probably due to the decrease in the mass-loss rate after the AGB phase, and by the

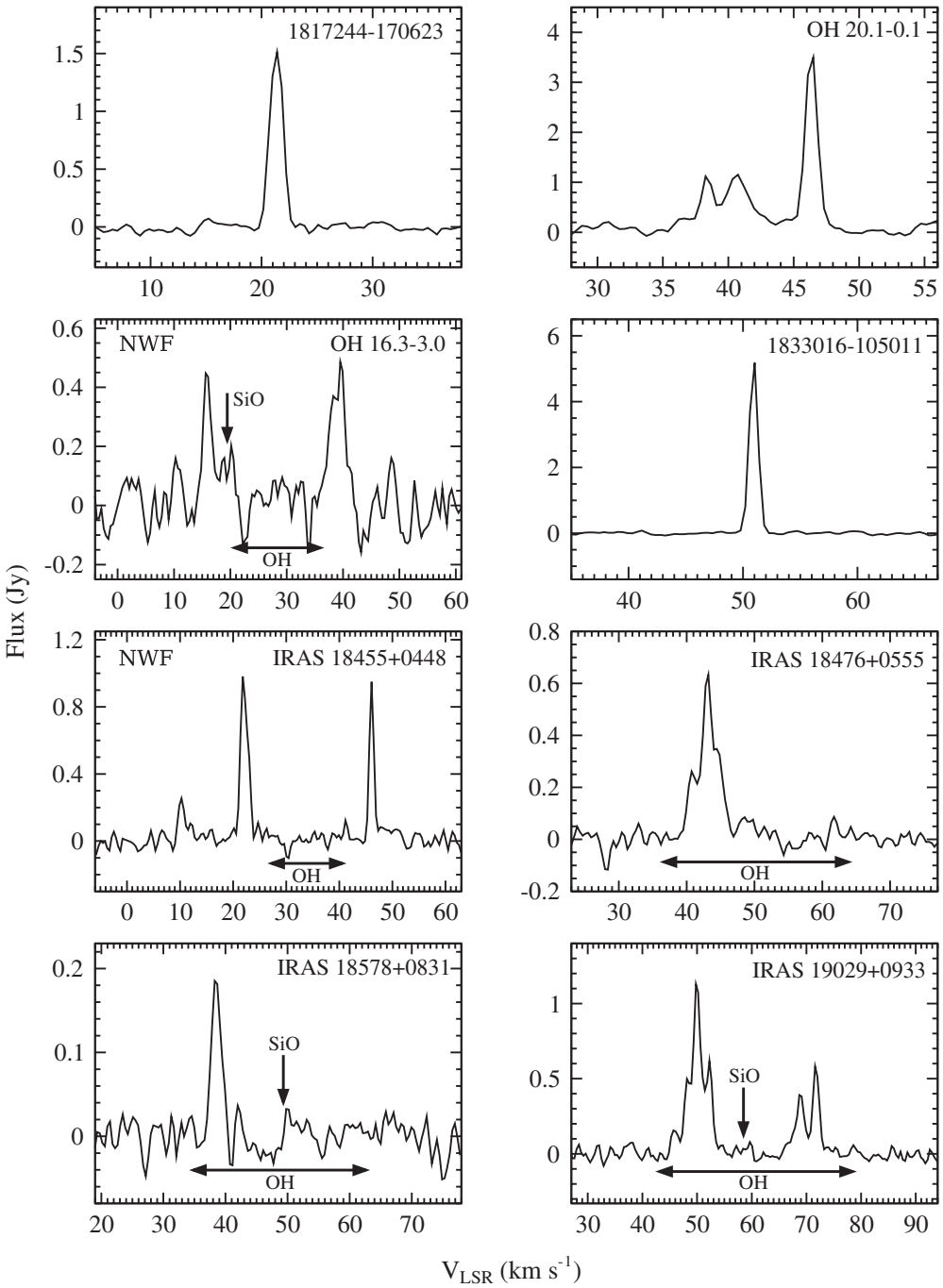

Figure 3. (Continued)

dissociation of the H_2O molecules into OH and H because of the ultraviolet radiation from the central star. The dissociation also happens at a larger distance from the photosphere, but this time it is due to external ultraviolet radiation (Habing 1996). Categories (d) and (e) consist of objects classified by more traditional ways, i.e., by their *IRAS* colors or the SiO maser properties. The detection rate is about 35% and 37%, respectively.

We have six additional objects from categories (f) and (g). These objects were non-detections in previous observations. We detected H_2O masers from four of these. It indicates that the sample selection criteria used by Lewis (1997) and Johnston et al. (1973) were indeed effective. However, Lewis (1997) achieved only a noise level of ∼0.3 Jy using the Haystack 37 m radio telescope, and for Johnston et al. (1973), almost 40 yr ago, the noise level was up to ∼12 Jy for a 5 minute integration using the 26 m reflector of the Maryland Point Observatory.

4.2. Objects with Larger Velocity Coverage of H_2O than OH Masers

Most of the detections in this project have an H_2O velocity coverage smaller than that of OH; this is the behavior of most circumstellar masers (see Section 1). We found four exceptions here. These are IRAS 15193+3132 (spectrum in Figure 4), IRAS 18056−1514, OH 16.3−3.0, and IRAS 18455+0448 (Figure 3). These objects show an H_2O velocity coverage that is larger than that for OH, and therefore they are WF candidates. Among

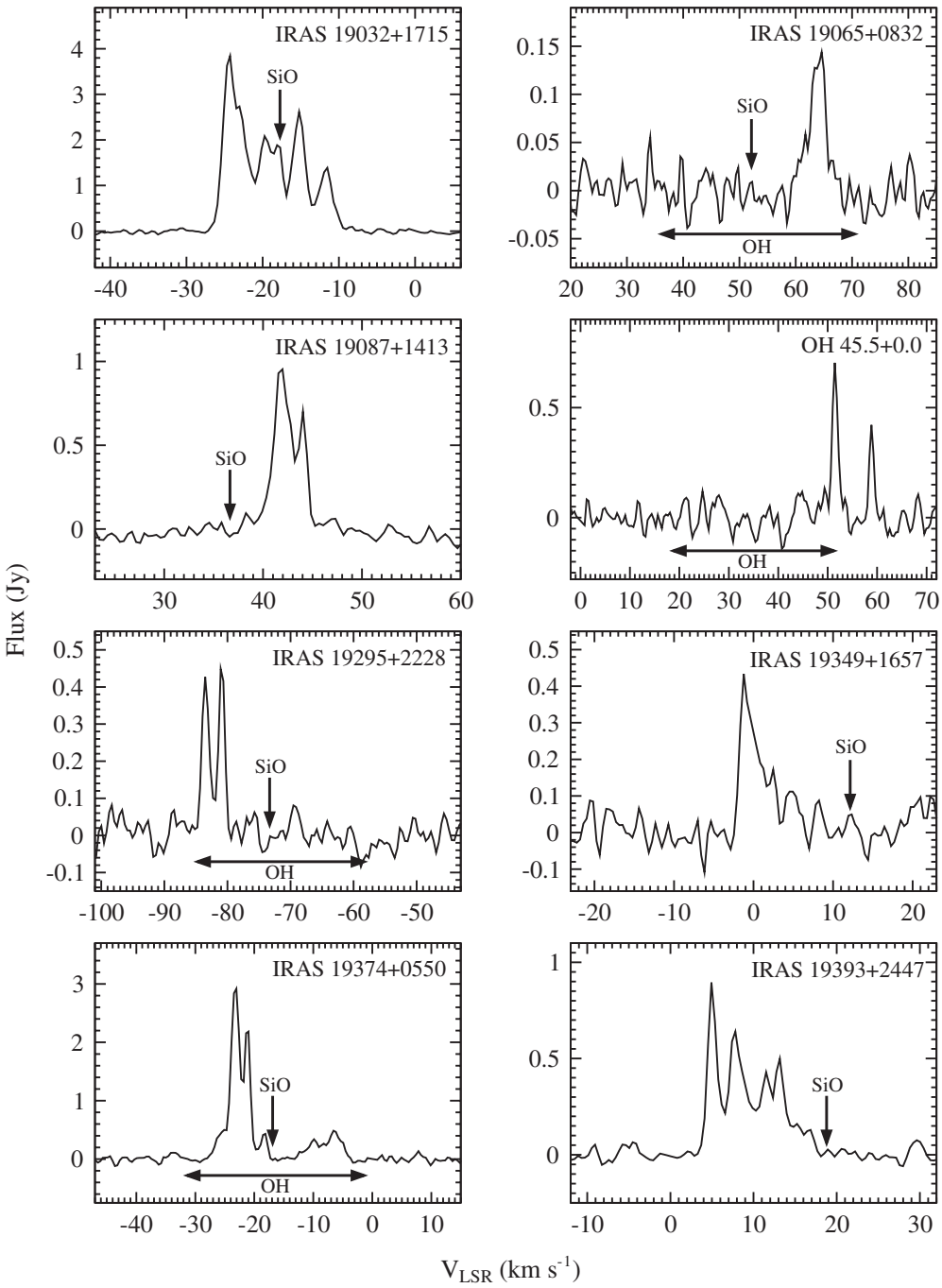

Figure 3. (Continued)

the four objects, IRAS 15193+3132 is a known H_2O maser source, while the other three are new sources. There is also another object, OH 45.5+0.0, with one of its two narrow H_2O features lying outside the OH interval (Figure 3), but this object is unlikely to be a WF (to be explained later in this subsection). We have looked at the infrared spectral energy distributions (SEDs) of the four candidates. All of them are characterized by a broad thermal emission feature in the mid- to far-infrared range. This is evidence for the presence of a thick envelope, as radiation coming from the central star is absorbed and re-emitted at longer wavelengths. A more extensive study on their SEDs will be presented in another paper (B. H. K. Yung et al. 2013, in preparation). The maser characteristics of the above objects are given below.

IRAS 15193+3132 (S CrB). This is a known H_2O maser source with a double-peaked profile (Valdettaro et al. 2001), which is suggested to be an AGB star with a pulsation period of about 360 days (Shintani et al. 2008). The current observation obtained a velocity coverage from about 1 to 11 km s^{-1}. This is a very bright source; the signal-to-noise ratio (S/N) is over 1000. Its OH maser was first detected by Lintel Hekkert et al. (1989), which showed a velocity coverage from -2.5 to 4.0 km s^{-1}. However, in recent OH observations obtained in the year 2012 using the Effelsberg 100 m telescope (data unpublished), we found that the OH coverage should be -5.0 to 5.5 km s^{-1} (Figure 4). Nonetheless, it is clear that the H_2O emission exceeds the OH interval on the redshifted side. A SiO maser is located at about -1 km s^{-1} (Kim et al. 2010). Regarding the

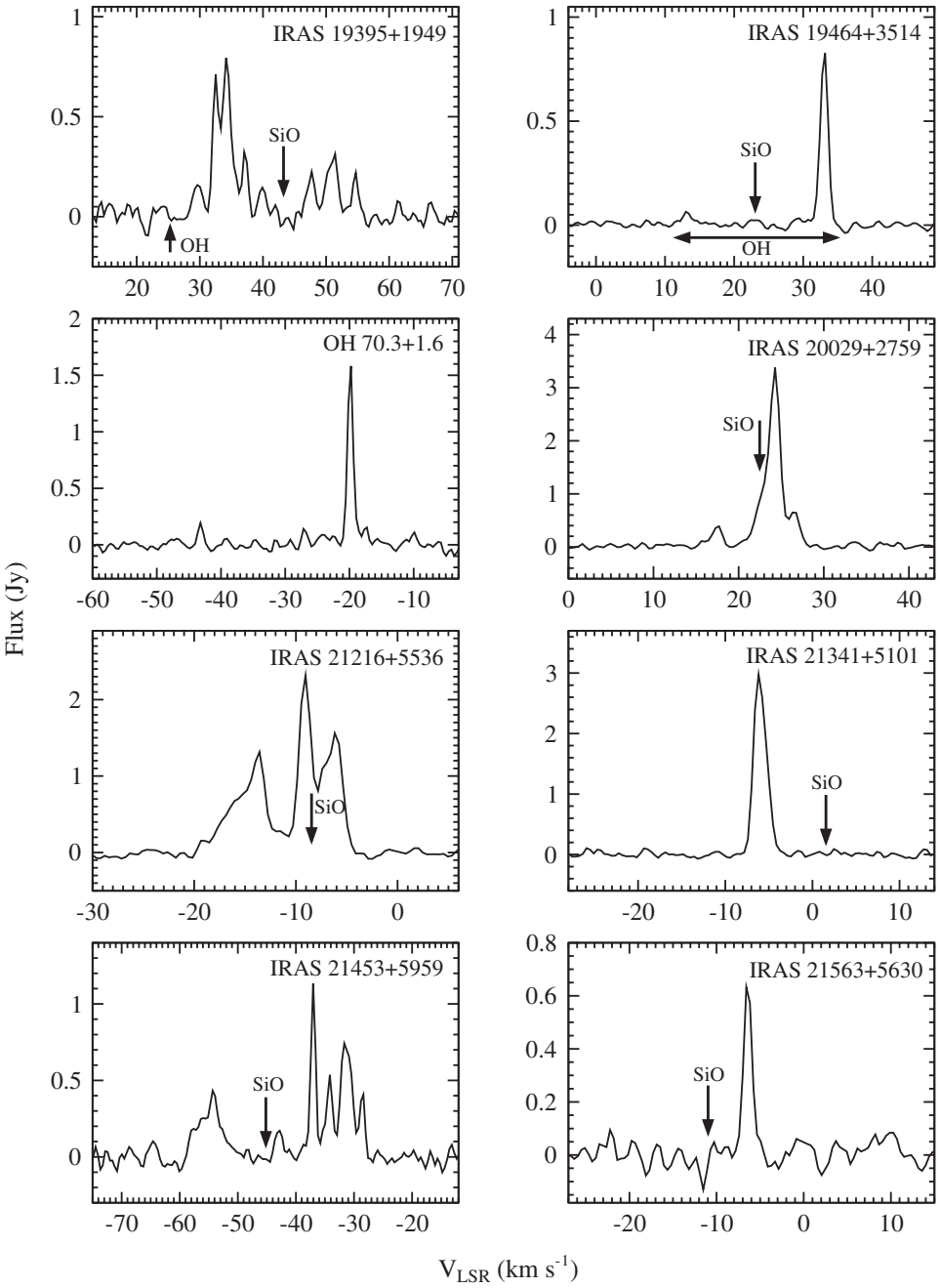

Figure 3. (Continued)

distance, the *Hipparcos* parallax given in the Astrometric Catalog (I/311/hip2) is 1.85 ± 1.19 mas (van Leeuwen 2007), implying a distance of about 540 pc, but with a large uncertainty. The total flux calculated from the infrared SED is about 1.0×10^{-10} W m^{-2}, corresponding to a luminosity of about 900 $L_{\odot}$. This value is too low for an AGB star (typically $\sim$8000 $L_{\odot}$), and we believe it is not accurate mainly due to the uncertainty in the parallax distance adopted. If the distance is confirmed to be reliable, then the low luminosity could be a consequence of a late thermal pulse (TP), when the star is becoming a "born-again AGB" star (e.g., Blöcker 1995). At the early stage of the late TP, the cold envelope is blown away, temporarily exposing the inner part of the star. A larger flux from shorter wavelengths is therefore expected. Nonetheless, at short wavelengths the influence of interstellar extinction is very significant. The total flux observed then decreases, and so does the implied luminosity.

IRAS 18056−1514. There are four H_2O maser peaks associated with this source; three of them are found within the OH velocity interval determined by te Lintel Hekkert (1991a) and one of them is outside. The S/N of the dimmest peak is about 21 (Figure 3). If we take the central velocity of the OH masers as the systemic velocity of the star, then the most blueshifted H_2O emission (at $\sim$36 km s^{-1}) implies a projected outflow velocity of about 23 km s^{-1}. The expected redshifted peak is missing, but since masers show variation, the peak is not detected probably because it is at its minimum. A SiO maser ($v = 2$, $J = 1$–0 transition only) is detected near the adopted systemic velocity, at about 60 km s^{-1} (Deguchi et al. 2000). The kinematical distance estimated using the systemic velocity and the galactic rotation

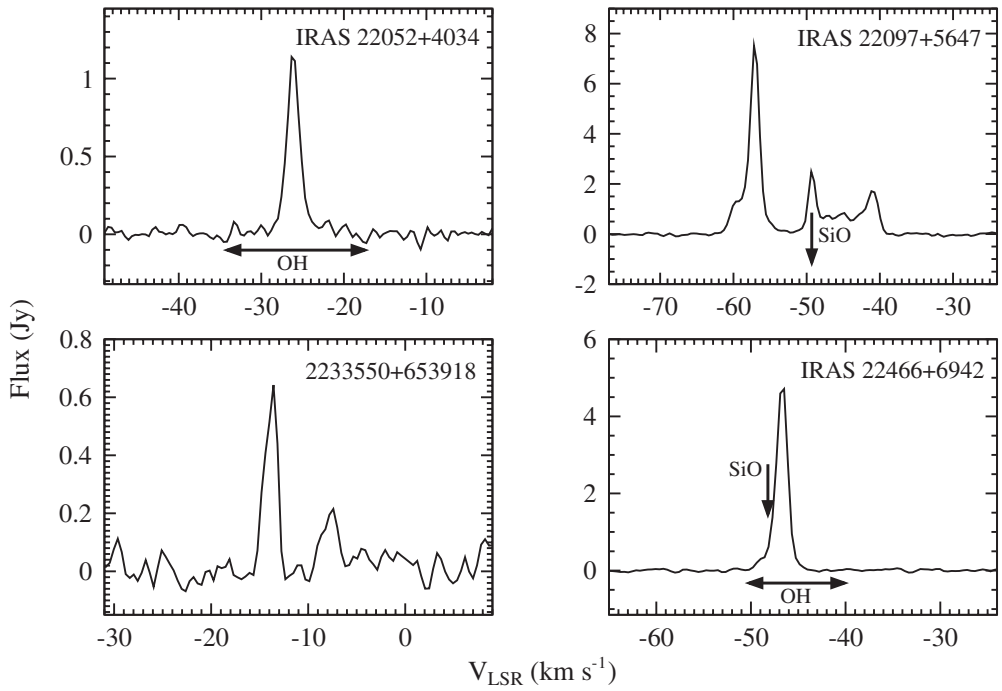

Figure 3. (Continued)

curve (Kothes & Dougherty 2007) is about 4.0 kpc. Note that the kinematical distance also includes a large uncertainty. The total infrared flux and the luminosity are about 4.6×10^{-12} W m^{-2} and 2300 $L_{\odot}$, respectively.

OH 16.3−3.0. This object shows a double-peaked profile for both H_2O and OH masers. The S/N of the H_2O peaks is about 5 (Figure 3). For OH, "wing-like" features were found in the outer side of both peaks (Sevenster et al. 2001). The velocity coverage between the two OH peaks is about 17 km s^{-1}, while for H_2O it is about 29 km s^{-1}. The OH peaks show the expansion velocity, so the "wings" are probably a sign of a fast outflow, and the most plausible case is a bipolar outflow. A SiO maser was found at about −19 km s^{-1}, with the 45 m telescope of the Nobeyama Radio Observatory (NRO) on 2012 March 18 (J. Nakashima 2012, private communication). It has to be noted that the SiO maser is not located at the supposed systemic velocity (i.e., the velocity halfway between the two OH peaks), but that it has a velocity similar to one of the OH peaks. The kinematical distance, total flux, and luminosity of the object are estimated to be 2.6 kpc, 9.0×10^{-12} W m^{-2}, and 2000 $L_{\odot}$, respectively.

IRAS 18455+0448. The OH maser profile of this object was first analyzed by Lewis et al. (2001). They found that the double-peaked feature was fading away over a period of 10 yr, and this object has been argued to be a very young post-AGB star. The OH velocity coverage is about 14 km s^{-1}. No H_2O masers were detected in the survey conducted by Engels & Lewis (1996). Our new H_2O spectrum (Figure 3) consists of two dominant peaks located on each side of the OH interval, and one additional blueshifted peak farther away from the systemic velocity. The S/N of the dimmest peak is about 7, and the total H_2O velocity coverage is about 39 km s^{-1}. No SiO masers were detected (J. Nakashima 2012, private communication). The near and far kinematical distances are 1.9 and 12 kpc, respectively. Lewis et al. (2001) suggested that in this case the far distance was more likely to be correct. This is because if one assumes the near distance, the luminosity would be very low (∼400 $L_{\odot}$), which contradicts the post-AGB star status that is supported by other evidence (e.g., by the behavior of the 1612 and 1667 MHz OH profiles). Adopting 12 kpc, the total flux and luminosity of the object are estimated to be 3.6×10^{-12} W m^{-2} and 16,000 $L_{\odot}$, respectively.

OH 45.5+0.0. The H_2O spectrum (Figure 3) shows two narrow peaks at about 51 and 58 km s^{-1}, and one of them is outside the interval covered by the OH masers (18–53 km s^{-1}). The H66α and H83β recombination lines are also detected within the 500 MHz bandwidth. When the spectra are set to the corresponding rest frequencies, both lines with broad profiles are centered at about 50 km s^{-1} (i.e., agree with the strongest H_2O feature).

In addition, new high-velocity H_2O maser components are found in the known WF IRAS 18286−0959 (Figure 4, and a close-up view in Figure 5), when comparing with our previous spectra obtained in years 2008 to 2010 with the Very Long Baseline Array (VLBA) and the NRO 45 m telescope. IRAS 18286−0959 has a precessing jet, which exhibits a unique "double-helix" pattern revealed by interferometric observations (Yung et al. 2011). The H_2O spectrum has an irregular profile with a lot of bright peaks. The new components are weak, but they are still well above the 5σ limit, with a noise level of about 5.31×10^{-2} Jy. The original velocity coverage is from about −60 km s^{-1} to 160 km s^{-1}. Now we see emission between −92 km s^{-1} and 171 km s^{-1}. The coverage has increased from 220 km s^{-1} to 263 km s^{-1}, surpassing IRAS 16342−3814 (∼250 km s^{-1}; Claussen et al. 2009). The velocity coverage is now the fourth largest among the 15 WFs. Only the H_2O emissions from IRAS 18113−2503 (∼500 km s^{-1}; Gómez et al. 2011), OH 009.1−0.4 (∼400 km s^{-1}; Walsh et al. 2009), and IRAS 18460−0151 (∼300 km s^{-1}; Deguchi et al. 2007) are distributed over a wider range. Therefore, the actual velocity of the jet could be faster than the currently adopted value (i.e., about 140 km s^{-1}; Yung et al. 2011), but probably due to the variability of the maser flux, these components were not detected before. Note that the observations committed in 2008–2010 have achieved a similar sensitivity as the

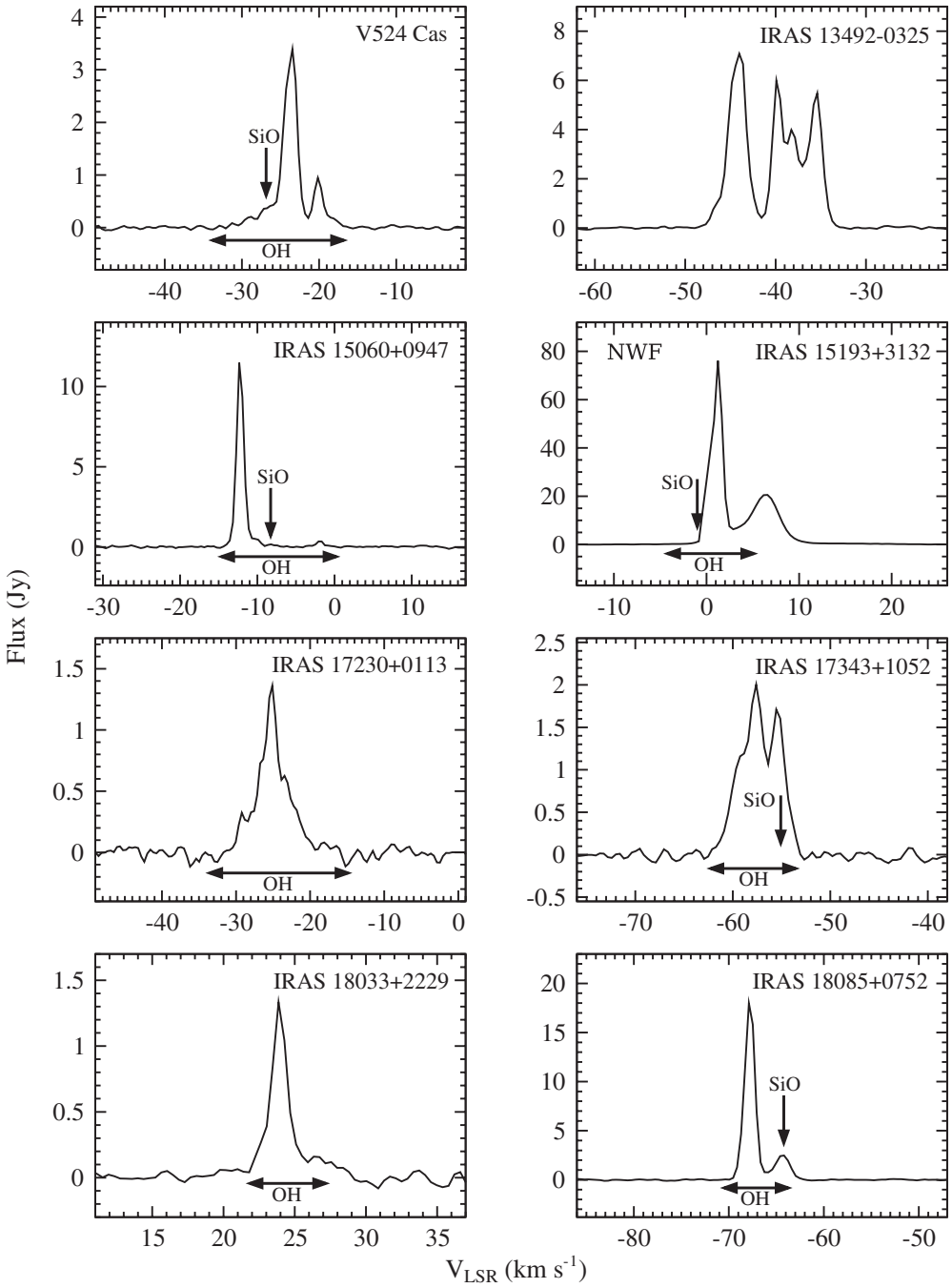

Figure 4. Spectra of known H_2O maser detections revisited. Some of them have new components detected; see Section 4.2 and the Appendix. The new "low-velocity" water fountain candidate (IRAS 15193+3132) is labeled "NWF."

current one (rms $\sim 10^{-2}$ Jy), so that the possibility of the new peaks being overlooked from previous work is excluded. On the other hand, the jet could indeed accelerate. However, that would imply an increase of >40 km s^{-1} of the jet velocity in 1–2 yr. It would be remarkable if true, because there were no such extreme accelerations ever found in evolved stars. Jet acceleration is possible as it is already found in the proto-PN CRL 618 (Sánchez Contreras et al. 2004) and another WF OH 12.9−0.9 (Boboltz & Marvel 2005), but there the acceleration is <10 km s^{-1} yr^{-1}. Since the jet of IRAS 18286−0959 is precessing, it is also possible that the velocity coverage is affected by the jet direction and shows time variation. However, according to our kinematical model (Yung et al. 2011), an increase of ∼40 km s^{-1} is difficult to explain by pure precession within 2 yr.

4.3. The Unclassified Object 2233550+653918

2233550+653918 is located in the post-AGB region of the *AKARI* two-color diagram (Figure 1). It has a near-infrared counterpart in the Two Micron All Sky Survey catalog, but not in the *IRAS* and *Midcourse Space Experiment* (*MSX*) catalogs. Its *WISE* image appears to be a stellar point source. No SIMBAD papers are found regarding this object, so it is completely new to us. It has a double-peaked H_2O maser profile spreading about 10 km s^{-1} (Figure 3). The S/N are about 16 and 6 for the blueshifted and redshifted peak, respectively. The true nature

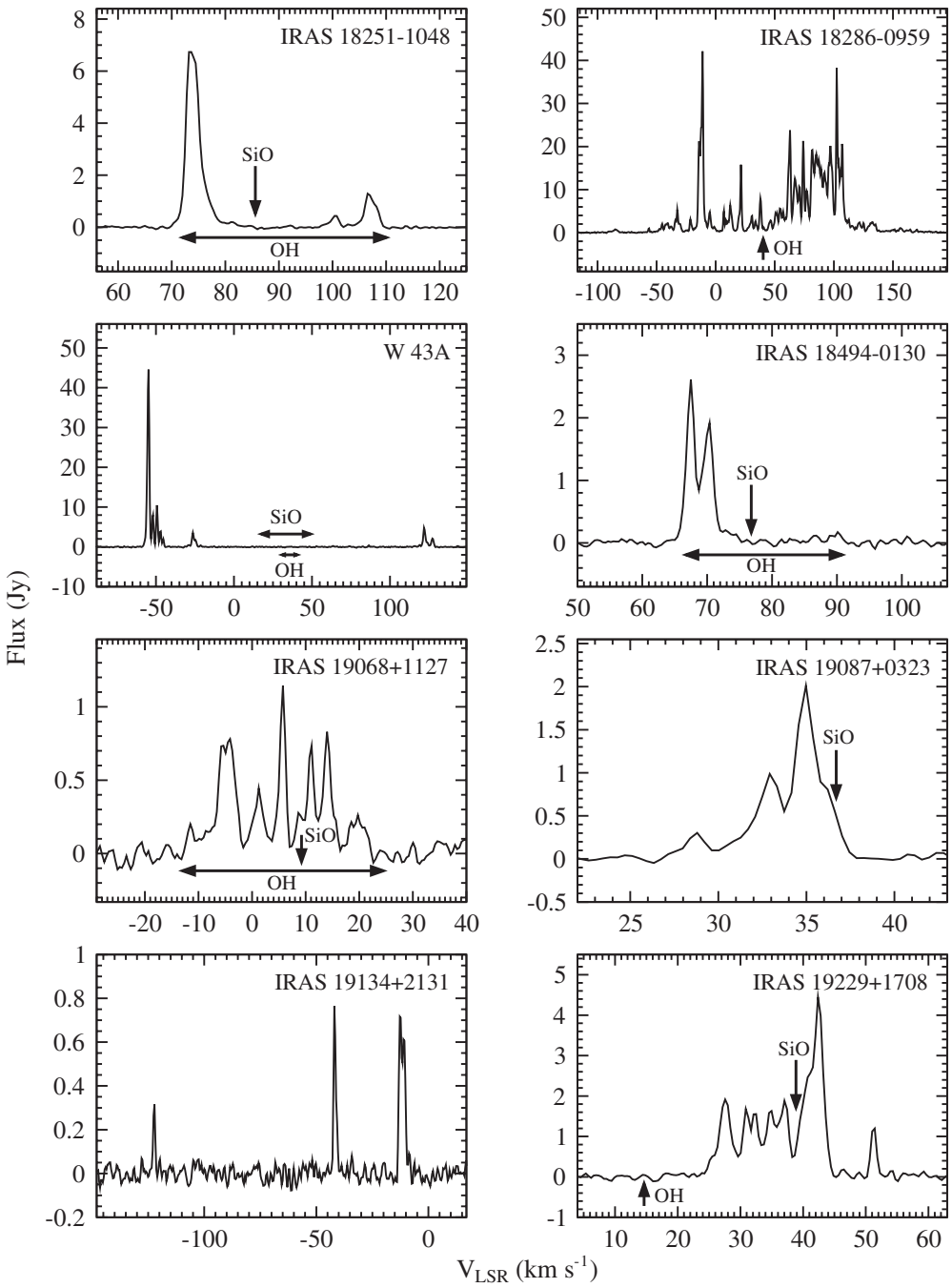

Figure 4. (Continued)

of this object is unknown but it might be an evolved star (more in Section 5.1). After the observation, we have found a few more objects with similar infrared properties (i.e., with post-AGB colors in the *AKARI* diagram; no *IRAS* and *MSX* counterparts, and no related studies are found). It shows that the high sensitivity of *AKARI* does enable us to find completely new maser sources, which could be post-AGB star candidates.

5. DISCUSSION

5.1. Confirmation of the Evolved Star Status

Some star-forming regions (SFRs) exhibit H_2O maser profiles or even infrared colors that resemble those of late-type objects such as post-AGB stars, so that misidentifications are possible. Furthermore, when the objects are close to the Galactic plane, contamination by other sources may also occur. Therefore, first of all, we have to consider the evolved star status of the newly found WF candidates (especially IRAS 18056−1514, OH 16.3−3.0, and IRAS 18455+0448). Their physical properties as WFs are discussed in later subsections.

We found that there are no other known red sources in *IRAS*, *MSX*, *AKARI*, or *WISE* catalogs except for the target sources within the main beam of the telescope, so the possibility of contamination is excluded. Then, we confirmed that there were no 21 cm continuum sources (i.e., H II regions) toward the corresponding directions of the four WF candidates (Condon et al. 1998). That implies these maser sources are not high-mass SFRs. There are also no reports on any OH masing low-mass SFR (Garay & Lizano 1999; Sahai et al. 2007), so the candidates are unlikely to be low-mass SFRs as well. The

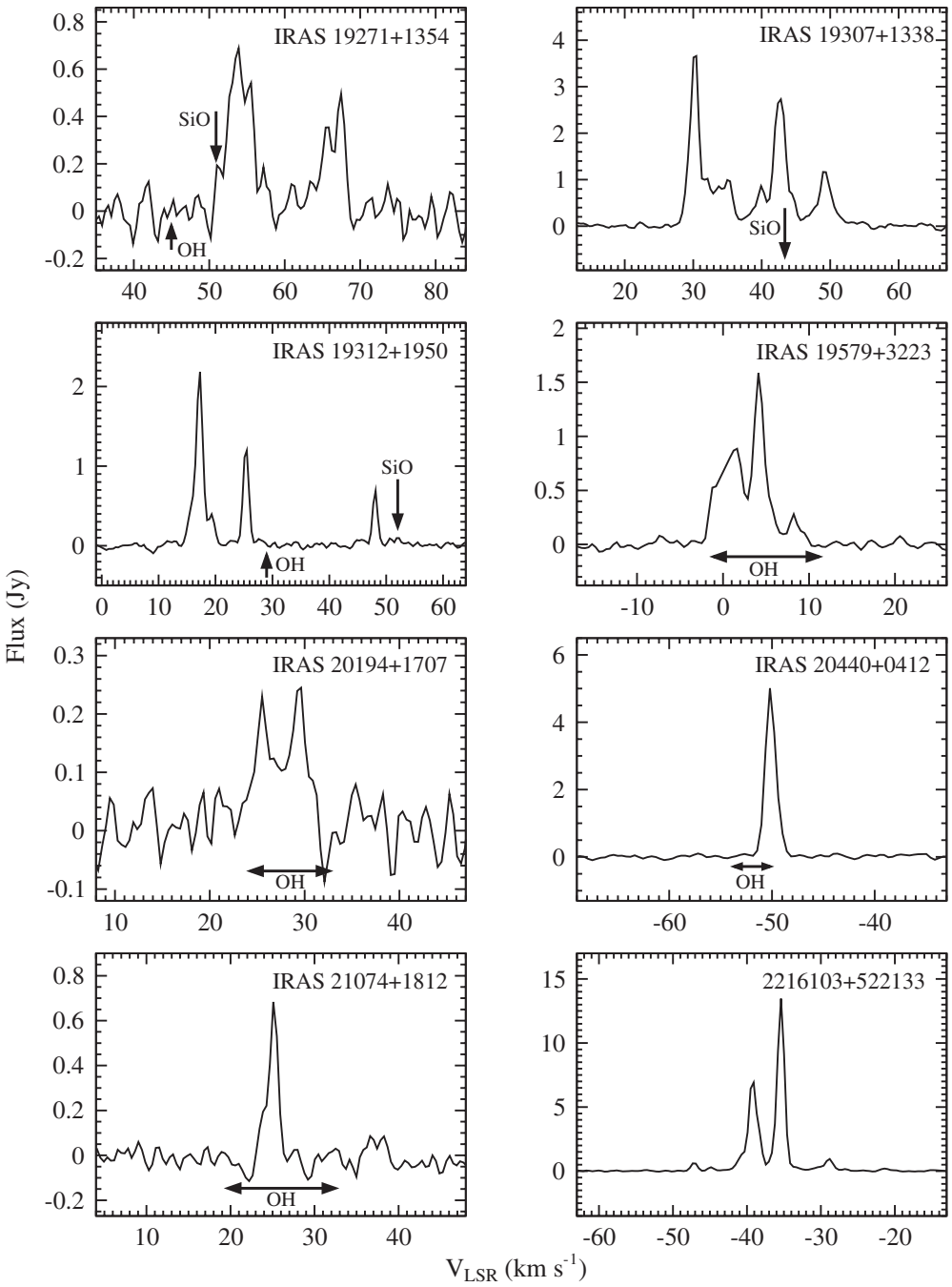

Figure 4. (Continued)

estimated luminosities given in Section 4.2 might not be accurate due to the uncertainties in the adopted distances. However, even in the extreme case of having 50% of distance uncertainty, the luminosities of all those objects are still brighter than the typical value ($<100\,L_{\odot}$) for a young stellar object. In addition, they appear as point sources in *MSX* and *WISE* mid-infrared images, which are very different from SFRs that normally show large irregular extended features.

Among the other new H_2O sources, 1817244−170623, OH 20.1−0.1 OH 45.5+0.0, and OH 70.3+1.6 are found to be lying in H II regions. OH 45.5+0.0 (Section 4.2) and OH 70.3+1.6 (the Appendix) are the only objects toward which the H66α and H83β recombination lines have been detected. These lines are detected in highly ionized regions. Note that some recombination lines are also found in PNe (e.g., Roelfsema et al. 1991). Nonetheless, OH 45.5+0.0 and OH 70.3+1.6 are unlikely to be PNe because of their highly irregular shape as shown in mid-infrared images. In addition, PNe are known to have a very low detection rate of H_2O masers due to the short lifetime (∼100 yr) of H_2O molecules in the PN environment (e.g., de Gregorio-Monsalvo et al. 2004). Thus, the above two objects are more likely to be SFRs. There are no detailed studies on 1833016−105011, but its mid-infrared images reveal a small nebulosity around the central object.

The rest of the new sources, including 2233550+653918 (Section 4.3), are most probably evolved objects because of their point-source-like appearance in mid-infrared images, as well as the non-detection of 21 cm continuum emission. The

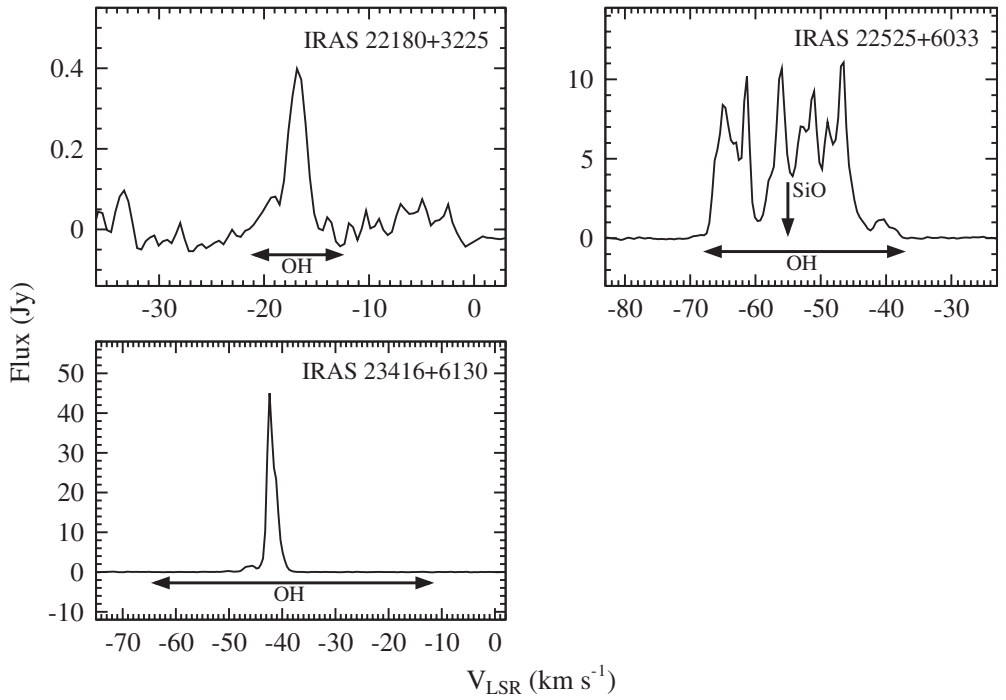

Figure 4. (Continued)

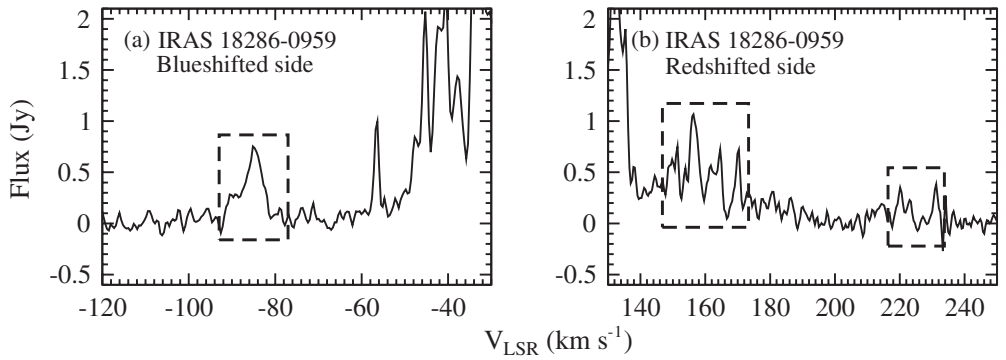

Figure 5. Close-up view of the H_2O maser spectrum of the WF IRAS 18286−0959 on the (a) blueshifted and (b) redshifted sides. The new velocity components are indicated by the broken-line boxes.

SiO maser detections toward some of the objects provide additional evidence for their evolved star status (e.g., Nakashima & Deguchi 2003a). The three exceptional cases where SiO masers are detected toward SFRs are Orion-KL (Kim et al. 2008), Sgr B2 (Shiki et al. 1997), and W51-IRS2 (Morita et al. 1992). Category (d) of our sample consists of some known SiO maser sources (see Table 1).

5.2. Properties of the New Water Fountain Candidates

In Section 1, we mentioned that the smaller H_2O velocity coverage of the low-velocity WFs could just be a projection effect on high-velocity jets, or that the jets could be intrinsically slower. For the four candidates reported in this paper, we suggest below that they are more likely to possess slow jets, and they are younger than other known WFs in terms of evolutionary status. Not knowing the true three-dimensional jet velocity yet, we will justify our idea by considering infrared colors and maser kinematics. Observations using very long baseline interferometry (VLBI) will be needed for further analysis.

5.2.1. AKARI and IRAS Colors

Based on the distribution of the AGB and post-AGB stars in Figure 1, we can assume a rough stellar evolutionary track in the diagram. This is because when an AGB star evolves further, its mass loss will create a very thick dust envelope which obscures the central star. The object will become very dim, or even unobservable, in the optical and near-infrared ranges. On the contrary, it becomes relatively bright in the mid-infrared due to the cold outer envelope. Hence, late AGB and early post-AGB stars normally show very red colors (e.g., Deguchi et al. 2007). As a result, the evolving AGB stars will move toward the "upper-right" direction in a two-color diagram, when their colors become redder. This evolutionary direction agrees with the model prediction by Suh & Kwon (2011). The same tendency is also noted in the *IRAS* two-color diagram presented by van der Veen & Habing (1988).

From Figure 1, the new WF candidates are expected to be less evolved than most of the other WFs, but at the same time, at least three of them have departed from the main cluster of AGB stars used in our sample. IRAS 18056−1514, OH 16.3−0.3, and

Table 3
Parameters of the H_2O Maser Detections

Object	$V_{b,p}$[a] (km s^{-1})	$F_{b,p}$[a] (Jy)	$V_{r,p}$[b] (km s^{-1})	$F_{r,p}$[b] (Jy)	$V_{b,e}$[c] (km s^{-1})	$V_{r,e}$[c] (km s^{-1})	I[d] (Jy km s^{-1})	rms (10^{-2} Jy)	Ref.[e]
IRAS 00170+6542	−63.4	2.21	...	...	−65	−58	4.80	3.23	New
V524 CAS	−23.5	3.36	...	...	−32	−16	10.08	2.46	1
IRAS 03461+6727	−37.9	4.22	...	...	−40	−36	5.60	4.61	New
IRAS 04209+4800	−21.0	7.55	...	...	−27	−11	19.26	2.75	New
IRAS 06319+0415	7.8	0.42	...	...	6	11	0.77	4.93	New
IRAS 13492−0325	−44.0	7.04	...	...	−47	−36	35.90	3.42	1
IRAS 15060+0947	−12.4	11.52	−2.0	0.32	−14	−1	15.26	4.48	2
IRAS 15193+3132	1.3	75.52	6.4	20.58	1	11	147.30	5.15	2
IRAS 17132−0744	4.1	0.74	9.9	0.22	2	12	1.60	4.70	New
IRAS 17171−0843	−9.5	0.70	...	...	−12	−7	1.25	4.86	New
IRAS 17230+0113	−25.1	1.38	...	...	−32	−20	5.31	4.16	2
IRAS 17343+1052	−57.6	1.98	−55.5	1.70	−63	−53	8.77	4.64	2
IRAS 18033+2229	23.9	1.34	...	...	22	26	2.08	4.48	2
IRAS 18050−0518	−27.2	1.02	...	...	−32	−20	3.26	4.83	New
IRAS 18056−1514	59.3	6.40	...	...	36	64	33.79	3.10	New
IRAS 18085+0752	−67.8	17.63	−64.2	2.46	−70	−62	29.92	4.32	2
1817244−170623	21.4	1.50	...	...	20	23	2.24	3.65	New
IRAS 18251−1048	73.5	6.75	106.6	1.28	70	110	27.14	3.39	3
OH 20.1−0.1	46.5	3.49	...	...	36	48	9.18	5.89	New
IRAS 18286−0959	−11.1	42.24	...	...	−92	171	1020.93	5.31	4, 5
OH 16.3−3.0	15.6	0.45	39.5	0.48	14	43	2.85	7.01	New
1833016−105011	51.0	5.18	...	...	50	52	4.96	3.49	New
W43A	−54.7	44.80	1.5	389.76	−58	129	127.14	6.34	6
IRAS 18455+0448	10.3	0.26	46.1	0.96	9	48	3.68	3.71	New
IRAS 18476+0555	43.2	0.64	...	...	40	48	2.02	2.46	New
IRAS 18494−0130	67.5	2.56	70.4	1.89	65	72	7.94	4.26	3
IRAS 18578+0831	38.7	0.19	...	...	37	41	0.35	1.86	New
IRAS 19029+0933	49.8	1.12	71.6	0.58	44	73	5.41	4.10	New
IRAS 19032+1715	−24.3	3.84	...	...	−27	−9	27.10	3.87	New
IRAS 19065+0832	64.6	0.13	...	...	58	68	0.48	1.92	New
IRAS 19068+1127	5.8	1.15	...	...	−13	22	10.24	4.83	2
IRAS 19087+1413	42.0	0.96	...	...	38	45	2.78	4.32	New
IRAS 19087+0323	35.0	2.02	...	...	27	38	5.79	3.42	7
OH 45.5+0.0	51.4	0.70	58.8	0.42	49	61	1.50	5.15	New
IRAS 19134+2131	−122.2	3.10	−12.7	0.70	−123	−8	3.42	2.91	8
IRAS 19229+1708	42.4	4.42	...	...	25	53	30.37	4.90	2
IRAS 19271+1354	53.9	0.67	67.5	0.48	50	69	3.97	7.07	2
IRAS 19295+2228	−81.1	0.45	...	...	−85	−80	1.18	3.39	New
IRAS 19307+1338	30.4	3.68	...	...	28	52	21.41	4.16	2
IRAS 19312+1950	17.3	2.11	48.2	0.70	14	49	7.01	3.10	9, 10
IRAS 19349+1657	−1.2	0.45	...	...	−3	3	1.18	4.29	New
IRAS 19374+0550	−23.0	2.91	−6.6	0.48	−29	−3	11.94	4.90	New
IRAS 19393+2447	4.9	0.90	...	...	3	17	4.51	2.59	New
IRAS 19395+1949	34.2	0.80	...	...	28	56	4.35	4.48	New
IRAS 19464+3514	13.0	0.06	33.2	0.83	12	35	1.38	1.44	New
IRAS 19579+3223	4.1	1.57	...	...	−2	10	6.24	2.98	2
OH 70.3+1.6	−43.2	0.19	−19.8	1.57	−45	−18	2.24	5.63	New
IRAS 20029+2759	17.7	0.38	24.3	3.39	15	28	8.38	4.77	New
IRAS 20194+1707	25.5	0.22	29.6	0.26	23	32	1.06	4.13	2
IRAS 20440+0412	−50.2	4.83	...	...	−52	−48	6.50	4.06	2
IRAS 21074+1812	25.1	0.77	...	...	23	27	0.96	3.71	7
IRAS 21216+5536	−9.1	2.30	...	...	−20	−4	11.74	4.03	New
IRAS 21341+5101	−6.2	2.98	...	...	−8	−6	2.78	4.16	New
IRAS 21453+5959	−37.0	1.12	...	...	−60	−27	6.14	4.00	New
IRAS 21563+5630	−6.6	0.61	...	...	−7	−5	0.77	4.26	New
IRAS 22052+4034	−26.3	1.15	...	...	−29	−23	2.34	3.30	New
IRAS 22097+5647	−57.2	7.52	...	...	−62	−39	26.98	3.78	New
2216103+522133	−35.4	13.47	...	...	−48	−28	32.64	3.42	2
IRAS 22180+3225	−16.8	0.38	...	...	−20	−15	0.90	3.33	7
2233550+653918	−13.6	0.64	−7.4	0.22	−16	−6	1.38	3.90	New
IRAS 22466+6942	−46.5	4.70	...	...	−50	−44	7.94	3.30	New
IRAS 22525+6033	−46.5	10.94	...	...	−68	−38	137.15	4.61	2
IRAS 23416+6130	−45.7	1.60	−42.4	44.80	−48	−39	89.50	3.26	11

Notes.
[a] V_{LSR} and flux density of the blueshifted peak of a double-peaked profile. For a single-peaked or irregular profile, the brightest peak is recorded in these two columns, whether or not it is really "blueshifted'.
[b] Same as above, but for the redshifted peak of a double-peaked profile, if it exists.
[c] V_{LSR} of the two ends of the whole emission profile. The cut-off is defined by the 3σ flux level.
[d] Integrated flux of the whole emission profile.
[e] References for known detections.
References. (1) Comoretto et al. 1990; (2) Valdettaro et al. 2001; (3) Engels et al. 1986; (4) Deguchi et al. 2007; (5) Yung et al. 2011; (6) Imai et al. 2002; (7) Engels & Lewis 1996; (8) Imai et al. 2007; (9) Nakashima & Deguchi 2000; (10) Nakashima et al. 2011; (11) Shintani et al. 2008.

Table 4
Parameters of the Non-detections

Object	rms (10^{-2} Jy)
IRAS 23575+2536	3.97
IRAS 01572+5844	4.96
IRAS 02547+1106	3.20
IRAS 03022+5409	3.94
IRAS 03206+6521	2.88
IRAS 05131+4530	2.75
IRAS 05284+1945	2.82
IRAS 05506+2414	3.23
IRAS 05552+1720	2.82
IRAS 06121+1221	3.65
IRAS 06238+0904	7.62
0759401+152312	9.28
IRAS 16030−0634	4.83
1611445+120416	3.97
IRAS 16131−0216	4.58
1644295+234759	4.19
IRAS 17055−0216	4.58
IRAS 17193−0601	4.45
IRAS 17308+0822	4.58
1744554+500239	2.91
1749069+080610	4.38
IRAS 17484−1511	6.02
IRAS 17531−0940	5.02
1758333+663759	3.26
1800071+663654	4.32
IRAS 18095+2704	4.16
1812063+065113	3.33
IRAS 18099−1449	5.18
IRAS 18100−1250	4.90
IRAS 18117−1625	5.09
IRAS 18118−1615	5.22
IRAS 18123+0511	3.87
IRAS 18127−1516	5.18
OH 15.7+0.8	5.98
1817340+100903	3.01
IRAS 18156+0655	5.15
OH 18.8+0.4	4.42
IRAS 18237+2150	4.45
IRAS 18236−0447	4.00
1827092+011427	5.02
IRAS 18245−0552	4.80
1829161+001822	5.09
1829553+004939	4.96
1830061+004233	3.81
IRAS 18273−0738	4.51
1834515−081820	4.29
1839230−055323	5.22
IRAS 18501+1019	3.36
IRAS 18517+0037	3.71
1854250+004958	4.35
OH 1854+02	3.42
IRAS 18587+0521	5.06
IRAS 18596+0605	4.96
IRAS 19010+0526	5.02
IRAS 19017+0608	4.96
IRAS 19024+1923	4.70
IRAS 19023+0745	4.90
IRAS 19027+0517	5.12
IRAS 19041+0952	5.12
IRAS 19044+0833	5.06
IRAS 19047+1539	4.80
IRAS 19055+0225	3.39
IRAS 19071+0625	5.54
1909599+043708	4.13

Table 4
(Continued)

Object	rms (10^{-2} Jy)
IRAS 19079+1143	5.38
1910544+012444	4.42
IRAS 19085+1038	4.74
IRAS 19114+0002	5.79
IRAS 19117+1107	3.94
1914408+114449	4.03
IRAS 19201+2101	3.14
IRAS 19231+3555	3.17
IRAS 19283+1421	3.20
OH 53.6−0.2	5.02
1932551+141337	4.29
IRAS 19309+2022	4.90
IRAS 19315+1807	4.96
IRAS 19323+2103	5.09
IRAS 19374+1626	5.12
IRAS 19414+2237	5.54
IRAS 19440+2251	4.90
1949296+312716	4.58
1952516+394326	5.22
IRAS 19583+1323	5.73
2001595+324733	4.06
IRAS 20010+2508	5.02
IRAS 20023+2855	3.68
IRAS 20021+2156	6.14
IRAS 20020+1739	6.50
2005300+325138	6.14
IRAS 20043+2653	3.87
2010236+462739	4.70
2012428+195922	4.99
2013579+293354	4.80
2015573+470534	4.61
IRAS 20156+2130	6.34
IRAS 20181+2234	6.14
2021328+371218	3.68
2021388+373111	5.82
IRAS 20215+6243	4.00
IRAS 20266+3856	3.46
IRAS 20305+6246	4.03
2032541+375128	4.35
2045540+675738	4.16
IRAS 20444+0540	5.31
2048166+342724	4.48
IRAS 20479+5336	4.16
IRAS 20523+5302	4.22
OH 85.4+0.1	3.94
IRAS 21000+8251	4.03
IRAS 20549+5245	4.19
2058537+441528	4.22
2058555+493112	4.13
2059141+782304	4.10
2119074+461846	4.61
IRAS 21509+6234	3.97
IRAS 21522+6018	4.06
2154144+565726	3.07
IRAS 21554+6204	3.52
2204124+530401	3.55
IRAS 22036+5306	2.43
IRAS 22103+5120	3.33
2219055+613616	4.26
2219520+633532	5.22
2223557+505800	5.44
2224314+434310	7.55
2235235+751708	3.94
IRAS 22345+5809	2.50

Table 4
(Continued)

Object	rms (10^{-2} Jy)
IRAS 22394+6930	3.81
IRAS 22394+5623	3.84
2251389+515042	4.86
IRAS 22517+2223	3.62
2259184+662547	3.74
2310320+673939	2.37
2312291+612534	2.53
2332448+620348	6.75
IRAS 23352+5834	5.06
IRAS 23361+6437	5.06
IRAS 23489+6235	3.78
IRAS 23554+5612	3.68
IRAS 23561+6037	3.71

IRAS 18455+0448 were originally selected using their *AKARI* colors, and incidentally, they are located in the upper-right corner of the AGB star region on the *AKARI* two-color diagram (see Figure 1), and they are not as red as the confirmed WFs in both color indices. The colors of these three candidates indicate that they could be transitional objects at the late AGB/early post-AGB stage. The remaining candidate, IRAS 15193+3132, lies in the AGB region of the *AKARI* two-color diagram, which is consistent with its suggested AGB status.

The *IRAS* two-color diagram suggests a similar story (Figure 2). IRAS 15193+3132 is found in region IIIa, while IRAS 18056−1514 and IRAS 18455+0448 are found at the boundaries between regions IIIa, IIIb, and VIb. OH 16.3−0.3 is missing because the 60 μm flux is not known. According to van der Veen & Habing (1988), variable stars with thick O-rich envelopes are found in regions IIIa and IIIb. These are very likely late AGB stars, where thick envelopes are formed due to mass loss. Region VIb contains variable stars with hot dust close to the photosphere, and cold dust at larger distances. These could be early post-AGB stars, where the steady spherical mass loss has been interrupted, and the dust far away from the central star has cooled down.

5.2.2. Maser Kinematics

If we believe that the new candidates are less evolved than other WFs, the next question concerns their jet velocities. The fact that the H_2O maser velocity coverage is larger than OH implies a physical differentiation of the faster H_2O maser flow (probably bipolar) from the circumstellar OH flow. From the spectra, we are not able to determine the three-dimensional velocity. Nonetheless, we can argue that the chance of the new candidates to be associated with high-velocity jets is rather low, by considering the orientation of the jet axes. Most WFs are found to have a three-dimensional jet velocity in the range of $100\,\mathrm{km\,s^{-1}} \leqslant V \leqslant 250\ \mathrm{km\ s^{-1}}$ (e.g., Imai et al. 2007; Walsh et al. 2009; Gómez et al. 2011). The projected velocity is given by $V\cos(i)$, where i (from 0° to 90°) is the inclination angle between the jet axis and the line of sight. If a low-velocity WF has an H_2O maser velocity coverage of about 30 km s^{-1}, then the projected velocity of the maser peaks will be 15 km s^{-1} (half of the total velocity coverage) off the systemic velocity. For jet velocities $V = 100$, 150, or 250 km s^{-1}, we obtain $i \approx 81°$, 84°, or 87°, respectively. Among the candidates that we have found, three of them have a velocity coverage of even less than 30 km s^{-1} (except IRAS 18455+0448). Therefore the inclination angle should be at least 81° for a 100 km s^{-1} jet, or even larger for higher velocity jets.

We can estimate the probability of seeing such a jet in the following way. Assume that there is no bias in the jet axis direction in the three-dimensional space, so that jets with different orientations are distributed uniformly across the sky. Then the probability $P(i_1, i_2)$ of observing a jet with an inclination angle between i_1 and i_2 (for $i_1 < i_2$) is given by

$$P(i_1, i_2) = \frac{1}{2\pi}\int_0^{2\pi}\int_{i_1}^{i_2} \sin(i)\, di\, d\phi, \qquad (1)$$

where ϕ is the azimuthal angle defined on the sky plane. For the extreme projection examples described above (i.e., $i_1 = 81°, 84°$ or 87°; $i_2 = 90°$), the probabilities calculated by the formula are about 17%, 10%, or 5%. On the other hand, the total number of WFs and WF candidates is 15+4 = 19. Thus, about $5/19 = 26\%$ of them are low-velocity WFs (including OH 12.8−0.9), which is higher than the calculated probabilities. Hence, the small H_2O velocity coverages are probably not caused by pure geometrical effects, and the objects are likely to have intrinsically slow jets.

According to the known cases of jet acceleration in OH 12.8−0.9 and CRL 618 (Section 4.2), we could assume that the very "first" bipolar outflow from a late AGB star might actually occur with a lower velocity that then gradually accelerates. This is consistent with our interpretation that the new WF candidates are younger and possess slower jets than other known WFs. The acceleration mechanism is still not clear, but there exist mechanisms like that proposed by the magnetocentrifugal launching (MCL) model (see Dennis et al. 2008 and references therein). The MCL model assumes the system has a rotating central gravitating object (the central star), which may or may not include an accretion disk. For the case where the disk is present (which is quite common in post-AGB stars), plasma is threaded by a magnetic field whose poloidal component is rotating in the same direction as the disk. The ionized gas of the disk is then subject to centrifugal force and accelerates. The gas is thrown out along the field lines. As the system expands, the toroidal component of the field dominates and the hoop stress (or circumferential stress) collimates the outflow. Note that a magnetic field ($B \approx 200$ mG at one position along the jet) has already been detected toward W43A, the first candidate of the WF class (Vlemmings et al. 2006). Therefore, it is possible that magnetic fields play a major role in collimating as well as accelerating the jets. If such acceleration is occurring, then the existence of the low-velocity WF candidates will imply that the dynamical age of WFs should be much larger than what has been expected (less than 100 yr; Imai 2007), because the current adopted value was estimated only with the high jet velocities.

Finally, regarding the SiO masers of the new WF candidates, we note that IRAS 18056−1514 has a SiO emission line at the systemic velocity. The fact that only the $v = 2$ line has been detected is consistent with the late AGB/early post-AGB phase prediction, as Nakashima & Deguchi (2003a) found that the SiO $v = 2$ line will become dominant as the objects get redder in their *IRAS* colors (i.e., more evolved objects). IRAS 15193+3132 also exhibits a SiO maser feature at about the systemic velocity, but only the $v = 1$ line has been measured (Table 1). The behavior of its SiO and OH masers also agree with its AGB status. It implies that the onset of an asymmetric outflow (as indicated by the H_2O and OH maser profiles) could actually happen at a stage much earlier than the post-AGB phase. The other two candidates show either SiO non-detections,

or the emission peak is seen off the systemic velocity. We suggest this is due to the preliminary morphological change, when the envelopes start to develop bipolarity. The SiO masers at this stage probably originated from an elongated region, and a double-peaked profile is expected even though we only have a single peak for OH 16.3−3.0. A similar example is the bipolar SiO outflow of the late AGB star W43A, which has been mapped with the Very Large Array (Imai et al. 2005). This stage, however, is expected to be short. As the star evolves further and the envelope detaches from the star, the SiO maser will disappear. This could be the case for IRAS 18455+0448 and the rest of the WFs. Therefore, considering all the properties discussed, the new WF candidates could be characteristic representatives of the short transition stage at the late AGB/early post-AGB phase, when the morphology of the envelopes starts to develop asymmetry.

6. CONCLUSIONS

We have conducted a 22 GHz water maser survey on 204 objects, mainly AGB and post-AGB stars, using various source selection criteria such as the *AKARI* two-color diagram. There are 63 detections and 36 of them are new, including an unclassified object, 2233550+653918, that was first identified by the *AKARI* observations. New high-velocity components are also found in the known "water fountain" IRAS 18286−0959. We have found four new candidates for this WF class, but having much smaller H_2O maser velocity coverage than other known examples. In principle, the smaller velocity coverage could just be a projection effect, or the objects are really associated with slower jets. From our statistics, we suggest that they are more likely to have intrinsically slow jets. They could be transitional objects undergoing a morphological change during the late AGB/early post-AGB stage. Studying the kinematical process occurring at this stage is helpful for us to understand the shaping of planetary nebulae. Nonetheless, the true status of the candidates can only be confirmed by interferometric observations, or by high-resolution infrared imaging, to see whether or not there are bipolar structures. The three-dimensional velocity of the outflow could also be determined by measuring the proper motions of the maser features with multi-epoch VLBI observations (e.g., Imai et al. 2002; Yung et al. 2011).

This work is supported by a grant awarded to J.N. from the Research Grants Council of Hong Kong (project code: HKU 704710P) and the Small Project Funding of the University of Hong Kong (project code: 201007176004). The results are based on observations with the 100 m telescope of the MPIfR (Max-Planck-Institut für Radioastronomie) at Effelsberg, and *AKARI*, a JAXA project with the participation of ESA.

APPENDIX

OTHER NOTABLE H_2O MASER DETECTIONS

There are some notable sources in addition to the new WF candidates found in this project, which will be briefly described below:

IRAS 06319+0415 (RAFGL 961). This is a well-known object suggested to be a massive protostar, made famous by the detection of the water ice vibrational band (e.g., Smith & Wright 2011). It is, however, the first time that an H_2O maser is found.

OH 70.3+1.6. It has two H_2O maser peaks. We suggest it is a high-mass SFR, as the H66α (22.364 GHz) and H83β (22.196 GHz) recombination lines are detected within our 500 MHz bandwidth. Both lines are centered at about -30 km s^{-1} (i.e., roughly halfway between the velocities of the two H_2O peaks). These lines only occur in highly ionized H II regions. The object also shows characteristic extended features in mid-infrared images, which agrees with the SFR assumption.

IRAS 19271+1354. This object has two clusters of H_2O peaks. The detection of the blueshifted cluster is reported in Engels & Lewis (1996), and the present observation is the first time that the more redshifted cluster is detected. A single-peaked feature was found in both the OH (Chengalur et al. 1993) and SiO (Nakashima & Deguchi 2003b) spectra, and the velocities of both emission peaks are lying outside the H_2O velocity range. The SiO maser resembles that of the new WF candidate OH 16.3−3.0 (i.e., significantly drifted away from the assumed systemic velocity). The object might have started to develop asymmetry in the very inner part of the envelope. Nonetheless, lacking fully convincing evidence, we conservatively do not suggest it is a WF candidate. To prove its true status, we have to at least detect both OH peaks and obtain accurate envelope expansion velocity.

IRAS 19295+2228. This object is identified as an OH/IR star, and it is visually close ($\sim$130″) to another object with a similar nature, IRAS 19296+2227. Their OH masers were observed in the same beam and recorded with the designation OH 57.5+1.8. However, Engels (1996) found that the two clusters of OH masers, with very different line-of-sight velocities, actually belong to two different sources. H_2O maser emission was found in IRAS 19296+2227, but not in IRAS 19295+2228 (Engels & Lewis 1996). Therefore, we present here the first detection of H_2O toward IRAS 19295+2228. In addition, Nakashima & Deguchi (2003a) searched for 43 GHz SiO masers toward both objects, but it was only found in IRAS 19295+2228.

IRAS 19312+1950. A new H_2O peak at 26 km s^{-1} is added to the known double-peaked profile of this source. Currently there are several speculations about the true nature of this peculiar object: it could be a post-AGB star embedded in a small dark cloud by chance, a red nova formed by a merger of two main sequence stars, or a coincidence of a background/foreground small dark cloud appearing in the direction of the *IRAS* source with the same V_{LSR}. Upon interferometric observations, it was shown that the two original H_2O peaks correspond to a possible bipolar outflow (see Nakashima et al. 2011 for a detailed study of this object). It is unclear how the new peak is produced in the system.

REFERENCES

Blöcker, T. 1995, A&A, 299, 755
Boboltz, D. A., & Marvel, K. B. 2005, ApJL, 627, L45
Boboltz, D. A., & Marvel, K. B. 2007, ApJ, 665, 680
Chengalur, J. N., Lewis, B. M., Eder, J., & Terzian, Y. 1993, ApJS, 89, 189
Cho, S.-H., & Ukita, N. 1996, A&AS, 115, 117
Claussen, M. J., Sahai, R., & Morris, M. R. 2009, ApJ, 691, 219
Comoretto, G., Palagi, F., Cesaroni, R., et al. 1990, A&AS, 84, 179
Condon, J. J., Cotton, W. D., Greisen, E. W., & Yin, Q. F. 1998, AJ, 115, 1693
David, P., Le Squeren, A. M., & Sivagnanam, P. 1993, A&A, 277, 453
de Gregorio-Monsalvo, I., Gómez, Y., Anglada, G., et al. 2004, ApJ, 601, 921
Deacon, R. M., Chapman, J. M., & Green, A. J. 2007, ApJ, 658, 1096
Deguchi, S., Fujii, T., Glass, I. S., et al. 2004, PASJ, 56, 765
Deguchi, S., Fujii, T., Izumiura, H., et al. 2000, ApJS, 130, 351
Deguchi, S., Nakashima, J., Kwok, S., & Koning, N. 2007, ApJ, 664, 1130
Deguchi, S., Nakashima, J., Miyata, T., & Ita, Y. 2005, PASJ, 57, 933
Deguchi, S., Shimoikura, T., & Koike, K. 2010, PASJ, 62, 525
Dennis, T. J., Cunningham, A. J., Frank, A., et al. 2008, ApJ, 679, 1327

Desmurs, J.-F. 2012, in IAU Symp. 287, Cosmic Masers—from OH to H_0, ed. R. S. Booth, E. M. L. Humphries, & W. H. T. Vlemmings (Cambridge: Cambridge Univ. Press), 1
Eder, J., Lewis, B. M., & Terzian, Y. 1988, ApJS, 66, 183
Engels, D. 1996, A&A, 315, 521
Engels, D., & Jimenez-Esteban, F. 2007, A&A, 475, 941
Engels, D., & Lewis, B. M. 1996, A&AS, 116, 117
Engels, D., Schmid-Burgk, J., & Walmsley, C. M. 1986, A&A, 167, 129
Fujii, T. 2001, PhD thesis, The Univ. of Tokyo
Galt, J. A., Kwok, S., & Frankow, J. 1989, AJ, 98, 2182
Garay, G., & Lizano, S. 1999, PASJ, 111, 1049
Gledhill, T. M., Yates, J. A., & Richards, A. M. S. 2001, MNRAS, 328, 301
Gómez, J. F., Rizzo, J. R., Suárez, O., et al. 2011, ApJL, 739, L14
Habing, H. J. 1996, A&ARv, 7, 97
Hu, J. Y., te Lintel Hekkert, P., Slijkhuis, F., et al. 1994, A&AS, 103, 301
Imai, H. 2007, in IAU Symp. 242, Astrophysical Masers and Their Environments, ed. W. Baan & J. Chapman (Cambridge: Cambridge Univ. Press), 279
Imai, H., Chong, S. N., He, J.-H., et al. 2012, PASJ, 64, 98
Imai, H., Diamond, P., Nakashima, J., Kwok, S., & Deguchi, S. 2008, in Proc. "The 9th European VLBI Network Symposium on the Role of VLBI in the Golden Age for Radio Astronomy and EVN Users Meeting," PoS(IX EVN Symposium), 060
Imai, H., Nakashima, J., Diamond, P. J., Miyazaki, A., & Deguchi, S. 2005, ApJL, 622, L125
Imai, H., Obara, K., Diamond, P. J., Omodaka, T., & Sasao, T. 2002, Natur, 417, 829
Imai, H., Sahai, R., & Morris, M. 2007, ApJ, 669, 424
Ita, Y., Deguchi, S., Fujii, T., et al. 2001, A&A, 376, 112
Izumiura, H., Deguchi, S., Fujii, T., et al. 1999, ApJS, 125, 257
Jewell, P. R., Snyder, L. E., Walmsley, C. M., Wilson, T. L., & Gensheimer, P. D. 1991, A&A, 242, 211
Jiang, B. W., Deguchi, S., & Ramesh, B. 1999, PASJ, 51, 95
Jiang, B. W., Deguchi, S., Yamamura, I., et al. 1996, ApJS, 106, 463
Johnston, K. J., Sloanaker, R. M., & Bologna, J. M. 1973, ApJ, 182, 67
Josselin, E., Loup, C., Omont, A., et al. 1998, A&AS, 129, 45
Kataza, H., Alfageme, C., Cassatella, A., et al. 2010, AKARI-FIS Bright Source Catalogue Release Note Version 1.0
Kim, J., Cho, S.-H., Oh, C. S., & Byun, D.-Y. 2010, ApJS, 188, 209
Kim, M. K., Hirota, T., Honma, M., et al. 2008, PASJ, 60, 991
Kothes, R., & Dougherty, S. M. 2007, A&A, 468, 993
Le Squeren, A. M., Sivagnanam, P., Dennefeld, M., & David, P. 1992, A&AS, 254, 133
Lepine, J. R. D., Scalise, E., J., & Le Squeren, A. M. 1978, ApJ, 225, 869
Lewis, B. M. 1994, ApJS, 93, 54
Lewis, B. M. 1997, AJ, 114, 1602
Lewis, B. M., David, P., & Le Squeren, A. M. 1995, A&AS, 111, 237
Lewis, B. M., Eder, J., & Terzian, Y. 1987, AJ, 94, 1025
Lewis, B. M., Eder, J., & Terzian, Y. 1990, ApJ, 362, 634
Lewis, B. M., Oppenheimer, B. D., & Daubar, I. J. 2001, ApJ, 548, 77
Likkel, L. 1989, ApJ, 344, 350
Likkel, L., Morris, M., & Maddalena, R. J. 1992, A&A, 256, 581
Lovas, F. J. 2004, JPCRD, 33, 177
Matsuura, M., Yamamura, I., Murakami, H., et al. 2000, PASJ, 52, 895
Morita, K.-I., Hasegawa, T., Ukita, N., Okumura, S. K., & Ishiguro, M. 1992, PASJ, 44, 373
Nakashima, J., & Deguchi, S. 2000, PASJ, 52, L43
Nakashima, J., & Deguchi, S. 2003a, PASJ, 55, 229
Nakashima, J., & Deguchi, S. 2003b, PASJ, 55, 203
Nakashima, J., & Deguchi, S. 2007, ApJ, 669, 446
Nakashima, J., Deguchi, S., Imai, H., Kemball, A., & Lewis, B. M. 2011, ApJ, 728, 76
Nyman, L.-A., Hall, P. J., & Olofsson, H. 1998, A&AS, 127, 185
Ott, M., Witzel, A., Quirrenbach, A., et al. 1994, A&A, 284, 331
Payne, H. E., Phillips, J. A., & Terzian, Y. 1998, ApJ, 326, 368
Roelfsema, P. R., Goss, W. M., Zijlstra, A., & Pottasch, S. R. 1991, A&A, 251, 611
Sahai, R., Morris, M., S. C. C., & Claussen, M. 2007, AJ, 134, 2200
Sahai, R., te Lintel Hekkert, P., Morris, M., Zijlstra, A., & Likkel, L. 1999, ApJL, 514, L115
Sánchez Contreras, C., Bujarrabal, V., Castro-Carrizo, A., Alcolea, J., & Sargent, A. 2004, ApJ, 617, 1142
Sevenster, M. N., van Langevelde, H. J., Moody, R. A., et al. 2001, A&A, 366, 481
Shiki, S., Ohishi, M., & Deguchi, S. 1997, ApJ, 478, 206
Shintani, M., Imai, H., Ando, K., et al. 2008, PASJ, 60, 1077
Sivagnanam, P., & Le Squeren, A. M. 1988, A&AS, 206, 285
Sivagnanam, P., Le Squeren, A. M., Minh, F. T., & Braz, M. A. 1990, A&A, 233, 112
Smith, R. G., & Wright, C. M. 2011, MNRAS, 414, 3764
Suárez, O., Gómez, J. F., Miranda, L. F., et al. 2009, A&A, 505, 217
Suárez, O., Gómez, J. F., & Morata, O. 2007, A&A, 467, 1085
Suh, K.-W., & Kwon, Y.-J. 2011, MNRAS, 417, 3047
Szymczak, M., & Gerard, E. 2004, A&A, 423, 209
Szymczak, M., & Le Squeren, A. M. 1995, MNRAS, 304, 415
Takaba, H., Ukita, N., Miyaji, T., & Miyoshi, M. 1994, PASJ, 46, 629
te Lintel Hekkert, P. 1991a, A&AS, 90, 327
te Lintel Hekkert, P. 1991b, A&A, 248, 209
te Lintel Hekkert, P., & Chapman, J. M. 1996, A&AS, 119, 459
te Lintel Hekkert, P., Versteege-Hansel, H. A., Habing, H. J., & Wiertz, M. 1989, A&AS, 78, 399
Valdettaro, R., Palla, F., Brand, J., et al. 2001, A&A, 368, 845
van der Veen, W. E. C. J., & Habing, H. J. 1988, A&A, 194, 125
van Leeuwen, F. 2007, A&A, 474, 653
Vlemmings, W. H. T., Diamond, P. J., & Imai, H. 2006, Natur, 440, 58
Walsh, A. J., Breen, S. L., Bains, I., & Vlemmings, W. H. T. 2009, MNRAS, 394, L70
Yamamura, I., Makiuti, S., Ikeda, N., et al. 2010, AKARI-FIS Bright Source Catalogue Release Note Version 1.0
Yung, B. H. K., Nakashima, J., Imai, H., et al. 2011, ApJ, 741, 94
Zapata, L. A., Menten, K., Reid, M., & Beuther, H. 2009, ApJ, 691, 332